Fabrication of high aspect ratio (HAR) atomic force microscope (AFM) tips and nano-pillar arrays using pseudo-Bosch and wet etching

by

Aixi Pan

A thesis

presented to University of Waterloo

in the fulfillment of the

thesis requirement for the degree of

Master of Applied Science

in

Electrical and Computer Engineering - Nanotechnology

Waterloo, Ontario, Canada, 2020

Author's Declaration

I hereby declare that I am the sole author of this thesis. This is a true copy of the thesis, including any required final revisions, as accepted by my examiners.

I understand that my thesis may be made electronically available to the public.

Abstract

This thesis is mainly focused on the research in the field of nanofabrication and application related to atomic force microscope (AFM) system. AFM tip is the most important part of AFM imaging to obtain the surface information by touching the substrate and “feeling” the force interaction. However, the scanned image using regular commercial tips is not accurate when scanning across areas with deep/tall and narrow structures. To overcome the drawbacks, high aspect ratio (HAR) tip was introduced to obtain high-quality and accurate images with high resolution and clear restoration. Several common fabrication techniques of HAR AFM tip including focus ion beam milling, electron/ion beam induced deposition, carbon nanotube tips and Nauganeedle method are reviewed, but batch production is hard to achieved due to the tips are fabricated one by one in these methods. Here we present a novel method based on dry etching to fabricate HAR AFM tips with high throughput, and some important steps such as electron beam lithography and etching process during the fabrication will also be discussed in this work.

The long-term goal of dry etching for our purpose is to have high etching rate, high etching selectivity to mask material, and controllable vertical profile with smooth sidewall, so non-switching (i.e. introduce SF_6 and C_4F_8 gas into the chamber simultaneously) pseudo-Bosch recipe was developed and optimized, to replace the standard Bosch process that gives wavy and rough sidewall. Moreover, when switching between SF_6/C_4F_8 etching and O_2 cleaning, that is, adding periodic oxygen (O_2) plasma cleaning step to the pseudo-

Bosch etching process, the etching rate of silicon structures can be significantly improved without any adverse effect. The obtained profile of pillars is slightly positively tapered which is optimal for HAR tips.

The fabrication of HAR tips is similar to that of HAR nano-pillars, and the same nano-pillars can be extended to the biomedical application of nanoneedles. As such, here we present a new method to fabricate ultra-high aspect ratio silicon nano-pillar arrays using reactive ion etching and subsequent sharpening/thinning down by wet etching, which features high viability and high throughput. The results show that the aspect ratio of the fabricated nano-pillars can be up to 125.

Acknowledgements

This work was carried out using the nanofabrication facility at Quantum NanoFab, WATLab and Giga-to-Nanoelectronics (G2N) Laboratory at University of Waterloo

I would like to acknowledge my supervisor, Prof. Bo Cui, for the wonderful opportunity to pursue my graduate studies and for his continuous guidance and support during this period.

I would also like to thank all lab colleagues and members from Bo Cui's research group for their assistance and support.

I would also like to acknowledge my reading committee members Prof. Irene Goldthorpe and Prof. Hany Aziz for their time and constructive feedback towards the completion of this thesis.

Table of Content

Chapter 3 HAR AFM tip fabrication

List of Figures

List of Tables

List of Abbreviations

AFM	Atomic force microscopy
BHF	Buffered hydrofluoric acid
C_4F_8	Octafluorocyclobutane
CH_3COOH	Acetic acid
CNT	Carbon nanotube
CVD	Chemical vapor deposition
DRIE	Deep reactive ion etching
EBID	Electron beam induced deposition
EBL	Electron beam lithography
FCCVD	Floating catalyst chemical vapor deposition
FIB	Focus ion beam
HAR	High aspect ratio
HF	Hydrofluoric acid
HNO_3	Nitric acid
HSQ	Hydrogen silsesquioxane
IBID	Ion beam induced deposition
IPA	Isopropanol
KOH	Potassium hydroxide
LMIS	Liquid metal ion source
MIBK	Methyl isobutyl ketone

MWCNT	Multi-walled carbon nanotube
PECVD	Plasma enhanced chemical vapor deposition
PMMA	Poly-methyl methacrylate
SEM	Scanning electron microscopy
SF_6	Sulfur hexafluoride
SOI	Silicon on insulator
SPM	Scanning probe microscopy
STM	Scanning tunneling microscopy
SWCNT	Single-walled carbon nanotube
TEM	Transmission electron microscopy
TMAH	Tetra methyl ammonium hydroxide

Chapter 1 Introduction to atomic force microscopy (AFM)

This Chapter gives a brief introduction, working principles and research motivations to AFM system.

1.1 Introduction

Microscopy offers a viable solution for exploring structures and properties of objects that are not within the resolution range of the unaided eye. With the development of innovative techniques, three main types of microscopy including optical, electron and scanning probe microscopy (SPM) come into view. Optical microscopy, also called light microscopy, is the most direct technique to view the sample through the magnification of lenses with visible light, but the obvious drawback to it is that the diffraction limits the resolution to approximately 0.2 micrometers [1]. Electrical microscopy offers much better resolution than optical microscopy, so scanning electron microscopy (SEM) and transmission electron microscopy (TEM) become two of the most common microscopy tools over the world in some essential fields for research. However, high cost and strict requirements of vacuum environment and conducting surface of sample limits some research. Scanning tunneling microscopy (STM) and atomic force microscopy (AFM) are two most common scanning probe techniques. Since STM was invented by Gerd Binnig et al. of the IBM Research Center in 1982 [2] and then the introduction of AFM in 1986 [3], more quantitative and qualitative information based on properties such as morphology, surface roughness, and texture are observed and analyzed. Table 1.1 represents the comparison of optical microscopy, SEM and SPM; it shows SPM can keep the performance of low cost and good resolution at the same time.

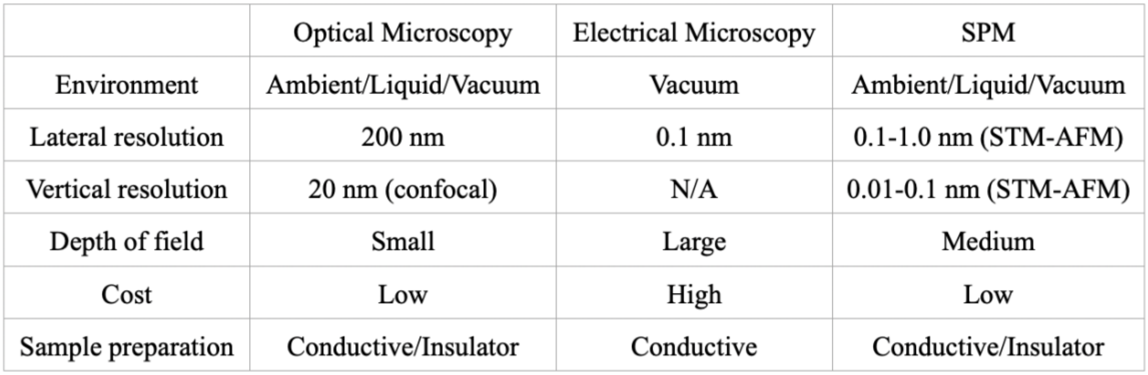

	Optical Microscopy	Electrical Microscopy	SPM
Environment	Ambient/Liquid/Vacuum	Vacuum	Ambient/Liquid/Vacuum
Lateral resolution	200 nm	0.1 nm	0.1-1.0 nm (STM-AFM)
Vertical resolution	20 nm (confocal)	N/A	0.01-0.1 nm (STM-AFM)
Depth of field	Small	Large	Medium
Cost	Low	High	Low
Sample preparation	Conductive/Insulator	Conductive	Conductive/Insulator

Table 1.1 Comparison of optical microscopy, SEM and SPM

As we mentioned before, both STM and AFM can be categorized as SPM, but they are quite different in use. STM works by scanning sample surface with a sharp metal tip by quantum mechanical tunneling effect and piezoelectric effect [4], and Figure 1.1 shows the schematic of STM. Electrons apply a quantum mechanical effect to tunnel from the tip to the sample surface, and the tip is moved by piezoelectric positioning. Then the feedback loop can monitor the tunneling current and the position of tip to generate a 3D image of surface topography. According to the STM system and working principle, two main limitations will affect the usage and results in research. The first one is the tip and material surface must be conductive and extremely clean, and the second one is that STM is very sensitive to mechanical noise and electrical noise.

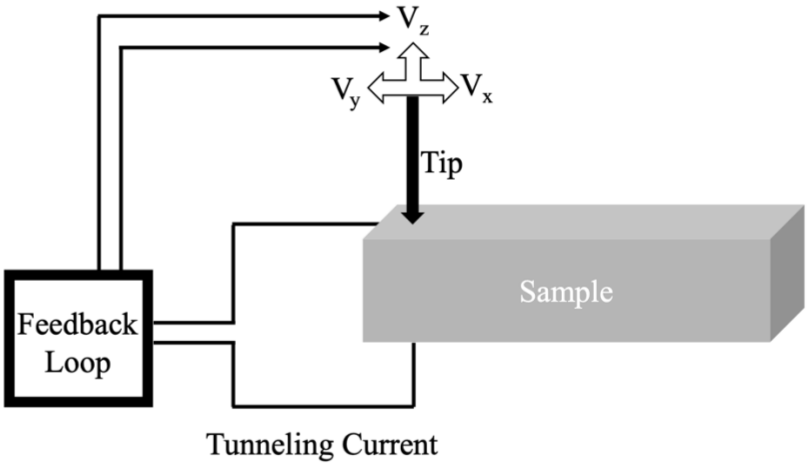

Figure 1.1 Schematic representation of STM system

Instead of measuring the tunnel current between one atom at the sharp tip apex and the sample surface in STM system, AFM measures the force between the tip apex and the sample surface. It means that the tip and sample can be non-conductive, and it can work in ambient, liquid, and vacuum conditions.

1.2 Working principles

1.2.1 Mechanism of AFM system

In AFM system, a flexible cantilever with a sharp tip is the most essential part, and all the information including the surface properties of a material is gathered by the changes of weak interatomic interaction between the sharp tip and the sample surface [5]. Figure 1.2 shows the structure of AFM [6], and it mainly consist of three parts.

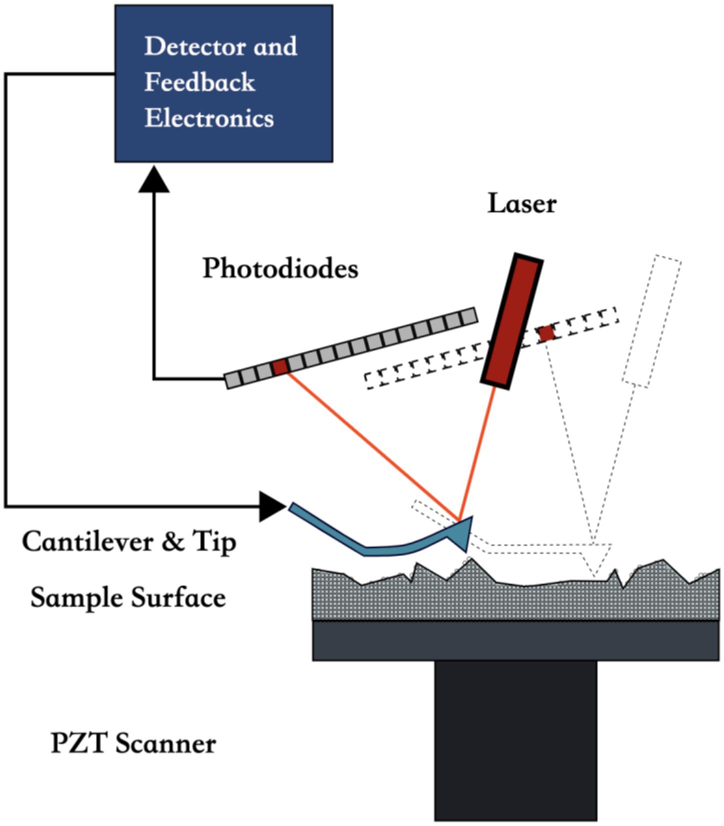

Figure 1.2 Schematic representation of AFM system

(adopted with permission from Ref. [5])

The first part is the force detection part. The van der Waals interaction between atoms and atoms is the dominant force in AFM system. Therefore, in system, the AFM probe with a cantilever holder, a cantilever and a sharp tip is used to detect the changes of interaction between atoms. The micro-cantilever is approximately 100-500 micrometer long and 500-5000 nanometer thick [7] with the sharp tip in the range of 3-20μm height, and both silicon and silicon nitride are good choices to be the materials of the probe. As different types of probes can be selected according to the characteristics of the sample and the mode of operation, the force detection part provides possibilities in different detecting environment.

The second part is the position detection part. After the cantilever bending due to the interaction between the tip and the sample, the position of the reflected light will be also changed when the laser is illuminated at the end of the micro-cantilever. In the entire system, recording and converting the offset into the electrical signal by the laser spot position detector is the most important process, which is called signal processing.

The third part is the feedback loop. After the signal is taken in via a laser detector, the feedback signal, which can be considered as an internal adjustment signal, drives a piezoceramic scanner moving appropriately to maintain a certain force between the sample and the tip.

1.2.2 Scanning modes

AFM can be operated in three conventional modes including contact mode, non-contact mode and tapping mode, and a new scanning mode named peek force tapping mode is recently introduced by Bruker [12].

1.2.2.1 Contact mode and non-contact mode

Conceptually, the most direct and convenience imaging mode is the contact mode in AFM system. During the entire scanning imaging process, the tip presses the specimen surface with an adjustable force, and the repulsive force can lead to the contact of the probe as shown in Figure 1.3(a).

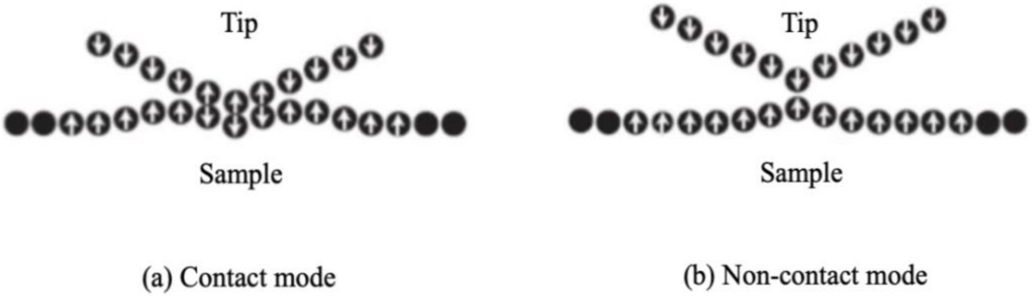

(a) Contact mode (b) Non-contact mode

Figure 1.3 Primary force in (a) Contact mode (b) Non-contact mode

Figure 1.4 also shows that repulsive force dominates when the gap between the tip and the specimen is small in contact mode, and the force increases when the gap becomes smaller [8][9]. In contact mode, constant force mode and constant height mode can be used in different situation. When the tip is kept at constant height, the scanning speed is high, and the sample must be relatively flat to avoid terrible damage. When the tip is kept at constant force, the tip is continually adjusted which can increase its service life comparing to constant height mode. However, the lateral force exerted on the sample surface is quite high, and this will lead to sample damage or the movement of special loosely attached objects. Soft sample is not advisable to be analyzed by the contact mode.

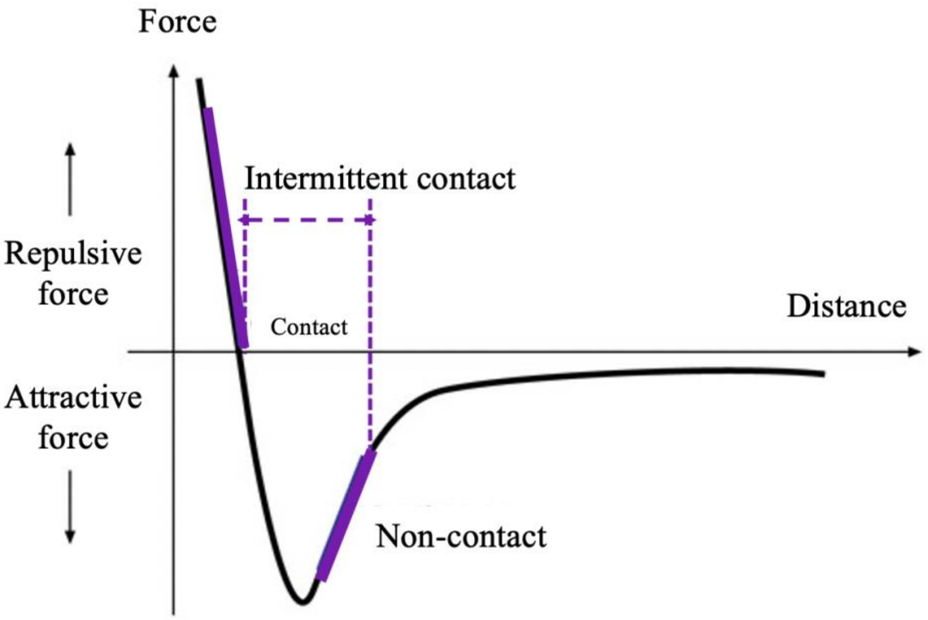

Figure 1.4 The curve of interatomic force versus distance

For the non-contact mode, the tip apex does not touch the sample surface, and the cantilever oscillates at a distance of 5-15 nm above the sample [10] to detect the attractive interaction mainly created by van der Waals force in Figure 1.3(b). Figure 1.4 shows that attractive force dominates when the gap between the tip and the specimen is small in contact mode, and the force decreases when the gap becomes larger. The van der Waals interaction is weak, thus the non-contact mode has the limitations including small distance between tip and sample, low amplitude and low scanning speed. Furthermore, one of the biggest drawbacks is the difficulty in achieving this mode in liquid environment or fluid layer. If the thickness of fluid layer goes beyond a certain range (5-10 nm), the tip will be trapped into it, and then force feedback will be inaccurate. In reality, the non-contact mode will stop working properly when the ambient relative humidity is well above 20%.

1.2.2.1 Tapping mode and peak force tapping mode

In tapping mode operation, the oscillating frequency of cantilever is close to the cantilever resonance [11] because of using amplitude modulation detection, and the cantilever amplitude is maintained by changing the tip-sample spacing. Tapping mode is a kind of combination of contact mode and non-contact mode as shown in Figure 1.4, and the force curve of tapping (intermittent contact) mode is constructed by summation of long-range attractive force and short-range repulsive force. The cantilever is released from a location within the range of z-piezo position with a triangular waveform applied to it in each contact. The attractive interaction dominates when the probe is approaching the sample until contact is happened, and repulsive force dominates from this point on. It results in less lateral damage than contact mode and more accurate imaging feedback than non-contact mode when moisture is present.

It is worth mentioning that an average response of many interactions is obtained instead of measuring a direct force in tapping mode, and the cantilever dynamics are complicated when cantilever is oscillated at its resonance frequency. This will lead to inherently unstable feedback situation and restrictions of the information beyond sample topography [12].

Peak force tapping mode has the similar fundamental principle to tapping mode, but it is operated in a non-resonant mode. The oscillating frequency is two orders below the cantilever resonant frequency to avoid the dynamics of a resonating system, and the oscillating amplitude is also much lower than the conventional tapping mode operation.

The lack of resonance facilitates the close following of the tip apex to the sample surface. Force curves for a silicon cantilever operated in peak force tapping mode are shown in Figure 1.5 [12]. This mode avoids unwanted resonances at the turnaround points in each contact, and the z-position is modulated by a sine wave instead of a triangular one in conventional tapping mode.

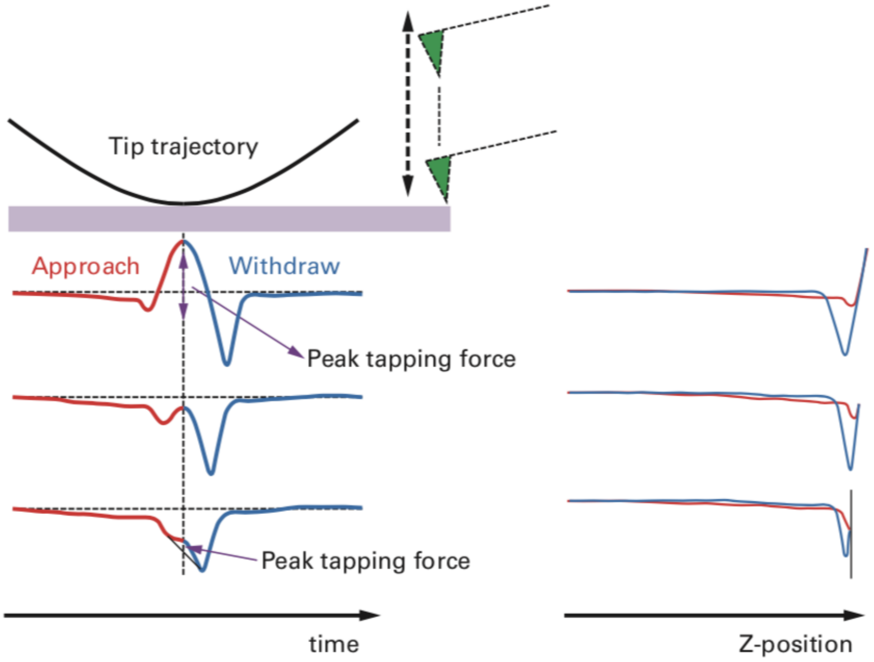

Figure 1.5 Force curves versus time and z-position for a silicon cantilever operated in peak force tapping mode [12]

According to the plot of force as a function of time, the peak tapping force can be measured when the horizontal dashed line is established as the zero-force reference (the force is zero when the tip is not interacting with the sample). The peak force in Figure 1.5

can be recognized below the zero-force reference, and it indicates that operating at very low forces is now possible. That is to say, soft samples like cells in a liquid environment can be applied to this mode. Comparing to the contact mode and tapping mode, the peak force tapping mode combines the benefits of less damaging lateral force and direct feedback with non-resonant mode [13].

1.3 Summary and research motivations

As mentioned before, three essential parts in a probe are tip, cantilever, and cantilever holder, and they make up the force detection part to sense the sample surface in AFM system. Figure 1.6 is a brief diagram of probe structure.

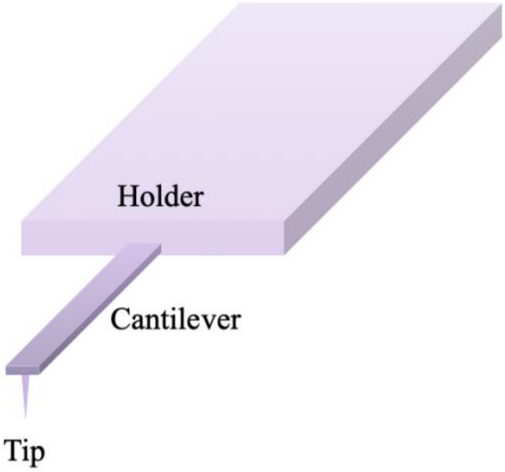

Figure 1.6 The structure of AFM probe including holder, cantilever and tip

Also, various materials are tried for fabricating AFM tips, and silicon is the most suitable and common material due to its low cost, high efficiency and availability. A good

SEM image of the silicon AFM probe which is captured during this research time is shown in Figure 1.7. According to the process of image formation in AFM system, the function of the tiny tip is extremely important, because it will affect the quality and resolution of the imaging results directly. Shaper tips lead to higher resolution [14], so the most effective way to improve the images of AFM is tip sharpening. For tip fabrication, high aspect ratio AFM tip fabrication is the most effective way to obtain the sharp tips.

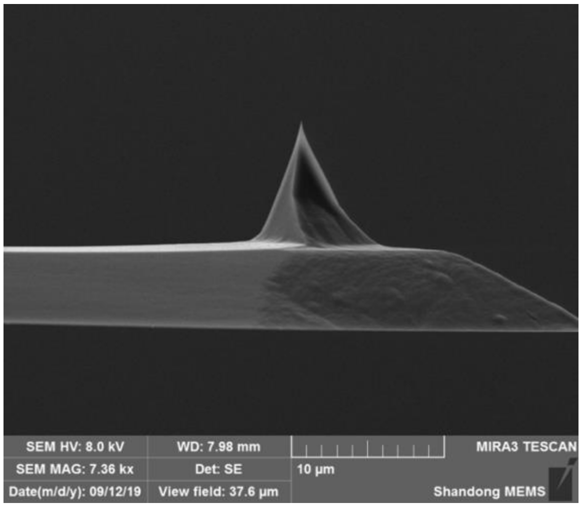

Figure 1.7 SEM image of a silicon AFM tip

Overall, this work mainly focus on the fabrication of high aspect ratio (HAR) silicon AFM tip, and two derivative topics including effect of oxygen plasma cleaning on non-switching pseudo-Bosch etching of high aspect ratio silicon pillars and fabrication of ultra-high aspect ratio silicon nanoneedle array will be covered later in Chapter 4 and Chapter 5 in details.

Chapter 2 HAR silicon AFM tip fabrication techniques

This chapter will mainly review several common fabrication techniques for HAR AFM silicon tip including focus ion beam milling, electron/ion beam induced deposition, carbon nanotube tips and Nauganeedle method.

2.1 Introduction to high aspect ratio AFM tips

Comparing with standard commercial silicon AFM tip, higher aspect ratio tip leads to higher resolution and clear restoration in imaging process. As shown in Figure 2.1, the final image is not accurate when AFM tip cannot reach to the bottom of the trench, so high aspect ratio tip is needed for better quality of scanning images. In usual, the length of high aspect ratio tip is three times longer than the diameter of tip base, so it can get into narrow gaps or special topography which will give more accurate results.

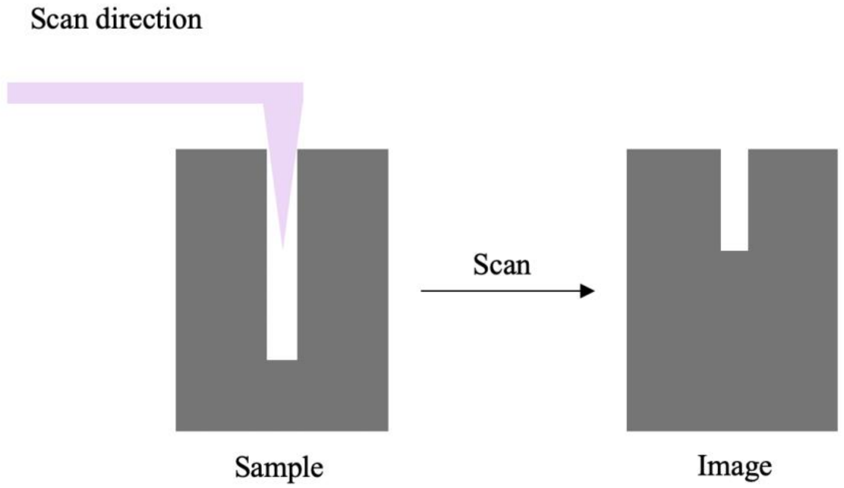

Figure 2.1 Schematic representation of AFM scanning process using normal tips

Four novel methods of fabricating the high aspect ratio AFM tips including focus ion beam milling, electron/ion beam induced deposition, carbon nanotube tips and Nauganeedle method are presented here.

2.2 HAR AFM tip fabrication by focus ion beam (FIB) milling techniques

Focus ion beam technique is a novel method that combines micro-analysis and machining, and it uses a liquid metal ion source (LMIS, usually gallium) as an ion gun with highly focused charged ion beam to scan or cut the substrate surface. This technique is similar to SEM technique, but it uses ion beam instead of electron beam. The size and the mass of ions are larger than electrons in the meantime, so the penetration into the substrate is shallower which makes them suitable for precise milling.

The experiment usually starts with the commercial silicon AFM tips or AFM probes with blunt tip [15][16]. To obtain a sharp tip, a small ring-shape area with inner radius to define the tip part is exposed to focused Ga^+ ion beam and milled away, and this process can be repeated to shrink tip size depending on needs. The tip apex radius is determined by the designed inner radius of pattern, and the sample can be rotated to desired position and angle to make the fabrication process controllable and precise. A research team from Southern Federal University published a high-performance AFM tip with apex radius of 5 nm in 2015 [17], and many companies such as NanoWorld [18] and NanoSensors [19] also offer AFM tips with high aspect ratio well beyond 10:1. SEM images of AR10-NCHR AFM tip by NanoSensors are shown here in Figure 2.2; the tip is FIB milled to achieve a high aspect ratio portion of 12:1 with sidewall angles approaching 90° [19].

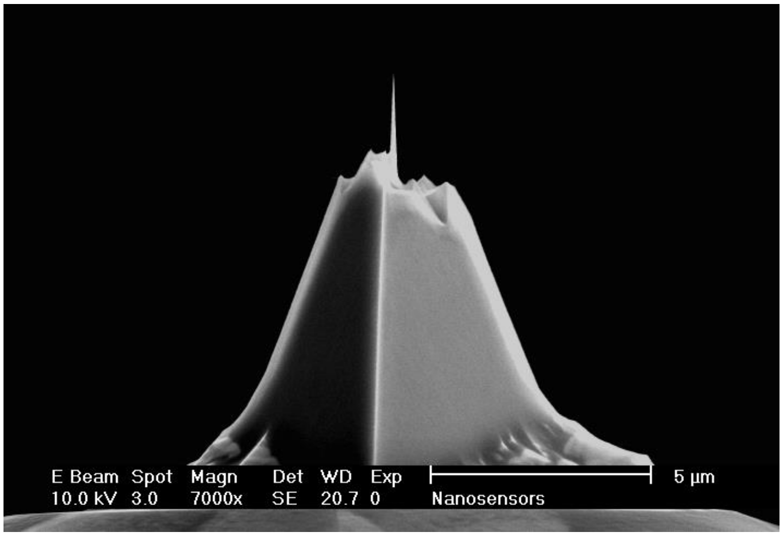

Figure 2.2 The front view of high aspect ratio AR10 AFM tip

(adopted with permission from Ref. [19])

However, the tips are processed one by one in a serial manner, and the operator has to focus and adjust the electron and ion beam before milling each tip. As a result, he overall FIB milling process for one tip takes tens of minutes that results in poor throughput and very high cost.

2.3 HAR AFM tip fabrication by electron/ion beam induced deposition (EBID/IBID) techniques

In addition to function of imaging and milling, focus ion beam can also be used to deposit materials contained in a precursor gas injected into the nearby area of the electron/ion gun excit and sample surface. This process is termed as ion beam induced deposition (IBID); and electron beam induced deposition (EBID) is similar to it except using focused electron beam. With the gaseous presursor is introduced into the vacuum chamber, the electron/ion beam scans the substrate surface and decomposes the gaseous materials into volatile and non-volatile species. The non-volatile species will be deposited on the scanning (target) area, and volatile species will be pumped away.

Many materials can be used to deposit by EBID/IBID, and the most common materials are carbon, silicon, oxide (SiO_x, TiO_x), and metals (Cr, Fe, Cu, Al, Au, Ni, Pt, W) [20]. Researchers at the University of Bath has fabricated thin carbon tip with the resolution of sub-20 nm by EBID in 2012 [21], but the fabrication time is quite long. Another example of HAR PtC AFM tip is shown in Figure 2.3 [22], where the IBID technique was used in the modification of tip apex. Research team of Nanda [22] achieved high aspect ratio tip with tip radius around 13 nm in 2015.

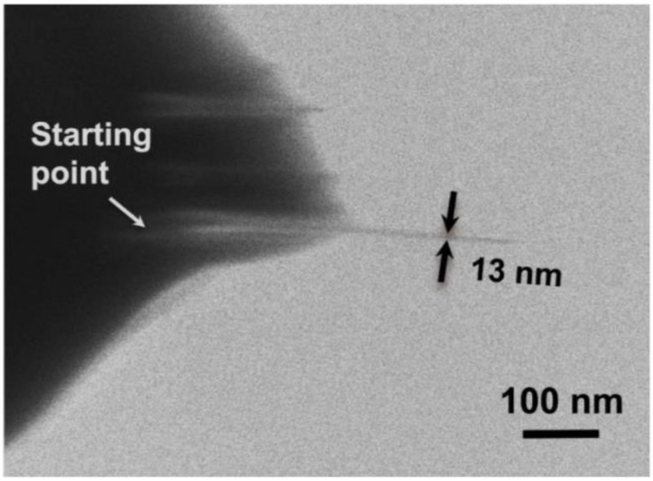

Figure 2.3 Modification of HAR tip apex by IBID grown PtC-nanowire

(adopted with permission from Ref. [22])

Compared with FIB milling, EBID/IBID techniques can create higher aspect ratio structures up to 1000:1. Although perfect profile of designed structures and accurate electron/ion beam deposition control can be achieved by EBID/IBID techniques, this technique is also costly and time-consuming.

2.4 Carbon nanotube (CNT) HAR AFM tip

Carbon nanotubes (CNTs), cylinder rolls formed by graphene sheets [23] in Figure 2.4, was first discovered by Lijima [24] in 1991, and they possess unique properties such as high mechanical flexibility and excellent thermal properties that makes CNTs have very long lifetime.

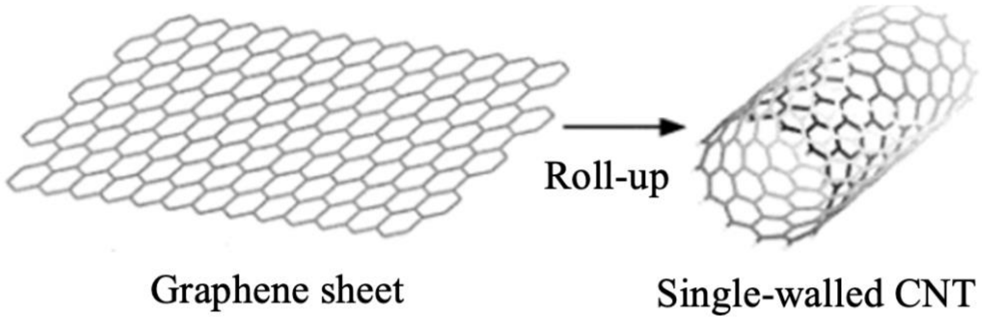

Figure 2.4 Schematic representation of the formation of S Single-walled CNTs

Single-walled CNTs (SWCNTs) is more popular than multi-walled CNTs (MWCNTs). The diameter of SWCNTs ranges from 0.4 nm to 3 nm, and the length of it can reach to 10 mm [25]. The controllable length and extremely high aspect ratio make SWCNTs good AFM tip material.

The most common methods to fabricate a CNT HAR AFM tips are attaching or growing by chemical vapor deposition (CVD) including thermal CVD, plasma enhanced CVD (PECVD) and floating catalyst CVD (FCCVD). The CNT AFM tip apex diameter can reach to around 10 nm which is fabricated by Nano Science & Technology team [26], and it offers smaller tip apex diameter with longer pillar height than the tips fabricate by EBID/IBID techniques. However, one of the biggest challenges is attaching or growing a CNT directly on tip apex with fixed position, orientation and length.

2.5 Needle-shaped HAR AFM tip

A relatively new method based on the self-assembly of silver-gallium alloy (Ag_2Ga) at room temperature [27] has been demonstrated and commercialized by NaugaNeedles company [28] in Figure 2.5. This process is similar to CNT growth, so the needle tips also have extremely high aspect ratio.

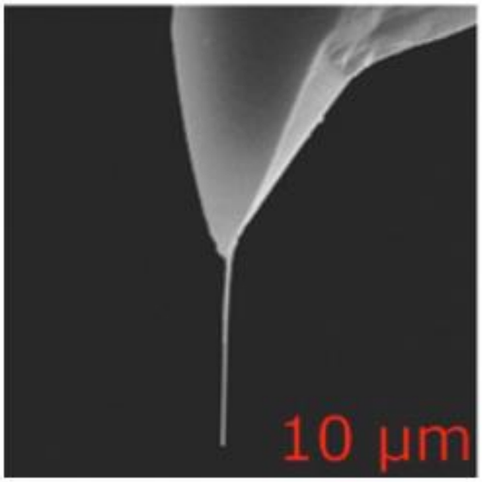

Figure 2.5 The profile of needle-shaped HAR AFM tip by NaugaNeedles [28]

However, the length of needle tips is hard to control due to the statistic nature of crystallization. The report shows the X-ray diffraction pattern of many needles grown simultaneously on a thin flat film instead of needles on real AFM tips, so the volume production method of fabricating needle-shaped HAR AFM tips with volume production is not realized yet.

2.6 Fabrication of HAR AFM tip by one-step lithography on bilayer resist and dry etching process

All the methods reviewed above have a common drawback of low cost-efficiency. In order to achieve high throughput of HAR AFM tips, a regular pyramid-shaped silicon tip can be sharpened by an oxidation under roughly 1000$_{o}$C and etching process by hydrofluoric acid [29]. The basic theory of oxidation sharpening is the silicon on curved surface (high-stress surface like concave or convex [29]) has slower oxidation rate. Apparently, silicon near the tip apex has the smallest radius of curvature, and silicon farther away from the apex has the larger radius of curvature [30]. That means silicon farther away from the apex will be oxidized more than the silicon near the apex, so the tip will be sharper after the removal of silicon oxide. This process is simple, and a wafer of tips can be processed simultaneously. However, the original cost of commercial tips is high, and the improvement of aspect ratio is hard to guarantee. Here we present a novel method to fabricate hundreds of high quality HAR AFM tips simultaneously on a wafer with low cost.

The fabrication of HAR AFM tip starts with a bare silicon wafer with chromium oxide (Cr_2O_3) hard mask on it, then the bilayer of electron beam photoresist including poly-methyl methacrylate (PMMA) and hydrogen silsesquioxane (HSQ) was spin-coated. Electron beam lithography was performed for the pattern of tip part and cantilever part. The cantilever pattern which is defined on HSQ is transferred to silicon wafer using standard Bosch process, and the tip part is defined on PMMA can be transferred by non-switching pseudo-Bosch process. The detailed background information and fabrication process will be introduced in Chapter 3.

2.7 Summary

This chapter reviewed several commonly used high aspect ratio (HAR) AFM tip fabrication techniques. To obtain high quality images and accurate information on sample topography, HAR AFM tip that can fully follow surfaces with deep/tall and narrow structures is needed. All the reviewed methods including FIB milling, IBID, EBID, CNT and needle-shaped tip by NaugaNeedles can be used for the fabrication and provide high-performance HAR tip, but batch production is not achieved as the tips are fabricated one by one in these methods. In order to increase the throughput with low cost, a novel method based on dry etching will be introduced in the next chapter.

Chapter 3 HAR AFM tip fabrication

In this chapter*, we present a novel and high throughput method (our method) to fabricate HAR AFM tips by using one-step lithography on bilayer of resists and dry etching process. Background information of techniques used in this work will be discussed here in detail.*

3.1 Electron beam lithography (EBL) system

The first EBL machines were developed from SEM in the late 1960s [31], and it is a useful technique for creating extremely fine patterns. The aim of using electron beam lithography is to create a template on mask, and then the pattern on template will be transferred into target layers by etching process. The main attribute of EBL is the high resolution when working with variety materials in nanofabrication, but it is complicated and expansive. The schematic of electron beam lithography system [31] is depicted in Figure 3.1.

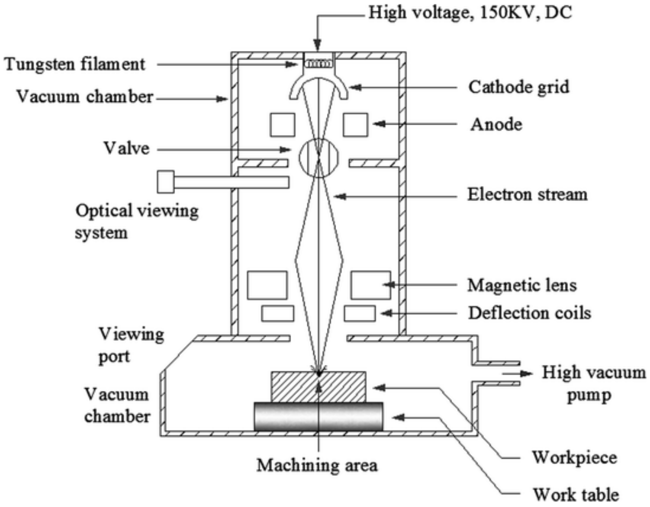

Figure 3.1 Schematic representation of electron beam lithography system

The EBL system includes three important parts including an e-beam generator, an electron accelerator, and electron-optical systems. After the electron flow is generated by the electron emission gun, it will be accelerated to obtain high kinetic energy. Then, the electron beam will be focused on one spot by a series of condenser lenses to achieve the final focused spot size of around 1nm, and the deflection coils scan the surface coated with electron beam resist [32].

3.2 Choice of electron beam resist

3.2.1 Poly-methyl methacrylate (PMMA)

Poly-methyl methacrylate (PMMA), also known as acrylic glass, is a macromolecule polymerized from monomer methyl methacrylate, and the structure of repeating unit and polymerization process is shown below in Figure 3.2.

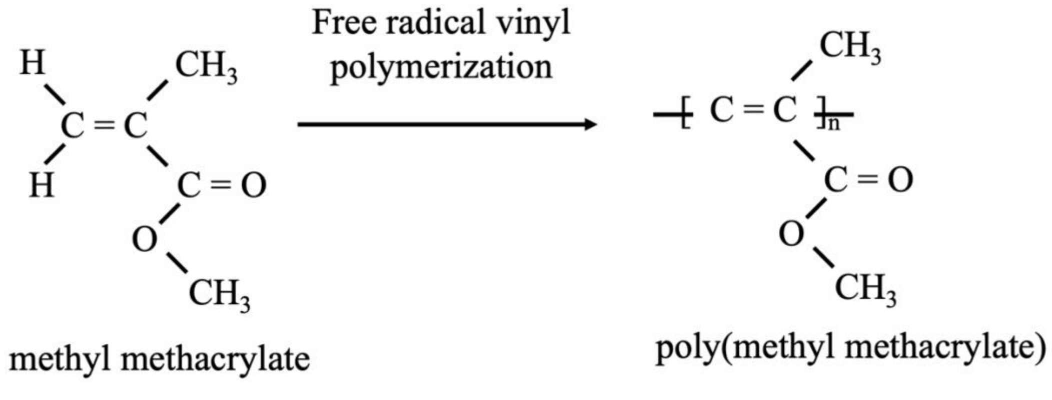

Figure 3.2 Schematic of the polymerization of methyl methacrylate

In nanofabrication techniques, PMMA has been used as a positive electron beam resist, offering extremely high resolution and ease of handling in a long time [33], and the positive characteristics occurs as PMMA polymer can be scissored into small chains under electron beam [33][34]. These short-length chains can be easily dissolved in an appropriate solvent such as methyl isobutyl ketone (MIBK) diluted with isopropanol. However, if the exposure dose is high or the exposure time is long enough, the carbonization [34] also occurs in these chains, and they will be crosslinked and transformed into an insoluble material, thus acting as a negative resist. The native tone character in high electron beam irradiation is used in this work, and the detailed information including the thickness of the resist and the dose for designed pattern will be detailed in chapter 3.6.

3.2.2 Hydrogen silsesquioxane (HSQ)

Unlike transforming from positive to negative tone under overexposure of PMMA, hydrogen silsesquioxane (HSQ) is a high-resolution negative-tone e-beam resist all the time. It is a highly ordered cage-like oligomer [35] as shown in Figure 3.3, and it can be dissolved in methyl isobutyl ketone (MIBK) and developed by alkaline developer such as AZ300 MIF developer (contains tetra methyl ammonium hydroxide, TMAH).

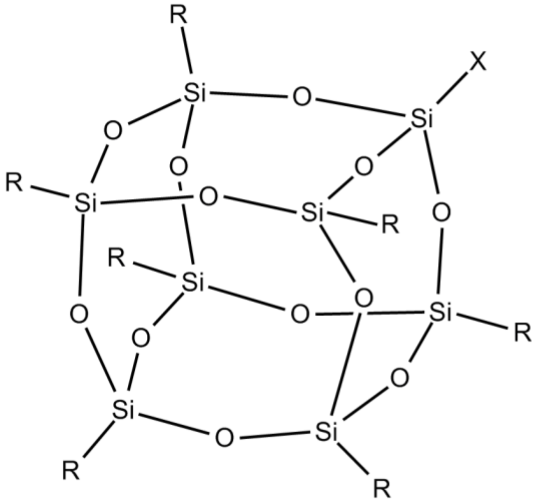

Figure 3.3 Schematic of the crystal structure of hydrogen silsesquioxane (HSQ)

HSQ is a good resist with extremely high resolution and large etching resistivity, and it was reported that the application of HSQ resist includes the fabrication of MOSFET gate with critical dimensions within 20nm [36], masks in bilayer lithography [37][38] and imprint templates [39]. However, one of the biggest drawbacks of HSQ is the shelf life. In this experiment, HSQ is stored at 5°C and it will expire within six months (depending on the storage condition), becoming gel-like substance. This limits the usage of HSQ in many aspects of research.

3.3 Etching techniques

The etching technique is used for etching or removing patterns from the surface of a substrate [40], and it can be divided into isotropic etching and anisotropic etching. Figure 3.4 shows the isotropic etching via a chemical process will etch in all directions within the substrate instead of a single direction, whereas the anisotropic etching etches in one single vertical direction [41]. Usually, most wet etching processes are isotropic and dry etching processes are anisotropic.

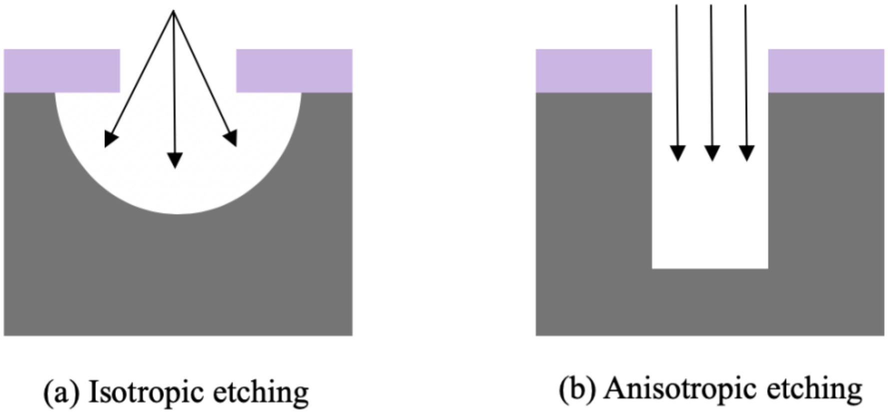
(a) Isotropic etching

(b) Anisotropic etching

Figure 3.4 Etching direction in (a) Isotropic etching (b) Anisotropic etching

3.3.1 Wet etching

Most wet etching processes are isotropic such as SiO_2 hydrofluoric acid (HF) etching and buffered hydrofluoric acid (BHF) etching [42]. There also exists wet etching process that is anisotropic, achieved such as with Si etching using hydroxides of alkali metal such as potassium hydroxide (KOH). Different silicon crystal orientation is shown in Figure 3.5. The crystal plane <111> has the highest surface density, so silicon etching rates at <111> plane is much slower than <110> and <100> plane [43]. These differences can lead to anisotropic etching on silicon wafer.

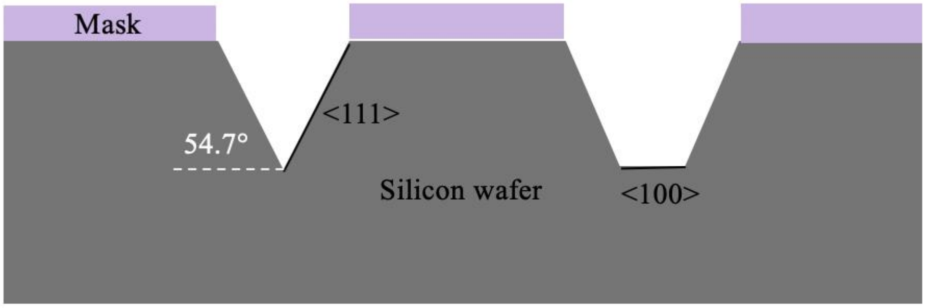

Figure 3.5 Wet etching process in different silicon crystal orientation

3.3.1.1 Chemical etching by HNO_3, HF and CH_3COOH/H_2O

Although wet etching process are not suitable for the fabrication of complex and extremely tiny structures or devices due to the isotropic nature and poor reproducibility [42][44], it is a low-cost etching method for high volume production.

An effective and convenient chemical etching process, by using the mixture of hydrofluoric acid (HF), nitric acid (HNO_3) and acetic acid (CH_3COOH) or water (H_2O), can sharpen/thin down silicon pillars. Here the etching is mainly determined by HF and HNO_3, and CH_3COOH or H_2O are diluents. The reaction mechanism of chemical etching is proceeded by the oxidation of silicon with HNO_3 first [45]:

$$\mathrm{Si} - 4\mathrm{e}^- \rightarrow \mathrm{Si}^{4+}$$

Here silicon dioxide is produced on the sample surface to prevent further oxidation. The process is followed by the dissolution of the oxide with HF:

$$\mathrm{SiO_2} + \mathrm{HF} \rightarrow \mathrm{SiF_6^{2-}}$$

where the product H_2SiF_6 is soluble.

The sharpening principle using this chemical etching system is shown in Figure 3.6. Apparently, the etching rate of the top part is faster than the bottom part of structures as the edge is exposed to solution in both vertical and lateral directions, hence high aspect ratio conic tip shape structures could be obtained.

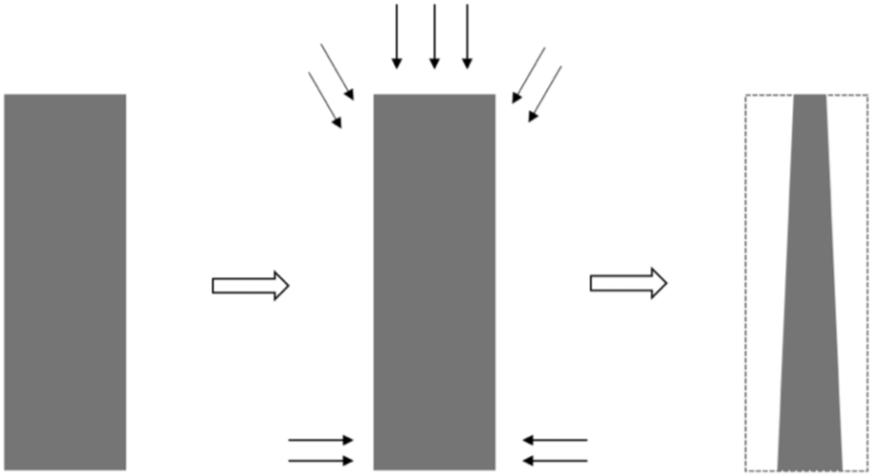

Figure 3.6 The principle of chemical etching system using HNO_3, HF and CH_3COOH/H_2O

3.3.2 Dry etching

Dry etching in Figure 3.7 was introduced to integrated circuit manufacturing in mid 1960s [46], and it is a revolutionary extension of etching technique by exposing the substrate material to free radicals and the bombardment of ions.

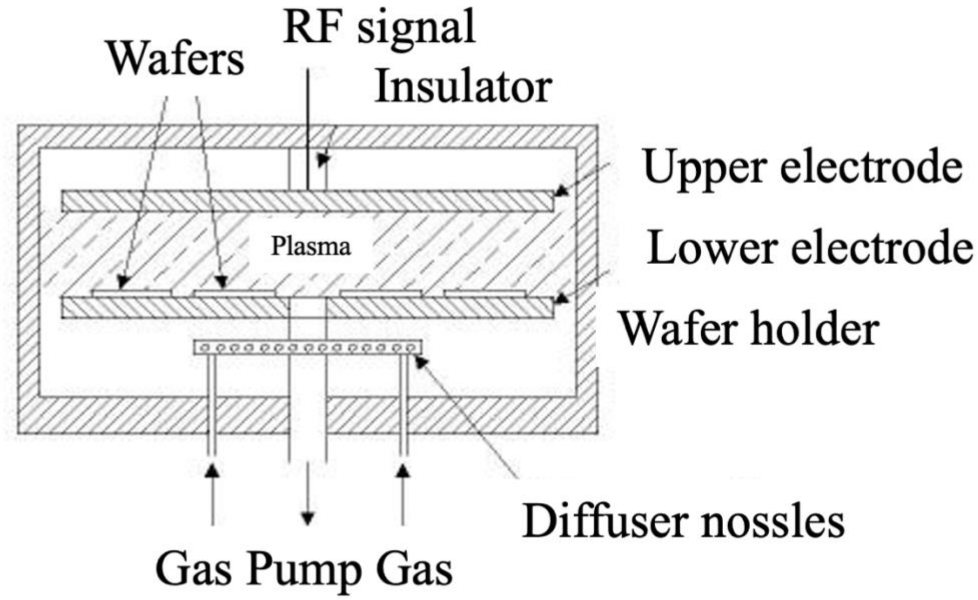

Figure 3.7 Schematic representation of dry etching process

The plasma of reactive gases such as chlorine and sulfur hexafluoride can be used [47]. When gases exist in the form of a plasma, it has two fundamental characteristics which are suitable for dry etching. The first one is the chemical reactivities of gases in the plasma is much stronger than that in the normal state, and the etching rate is faster if one selects gases suitable to the substrate materials. The second one is that the electric field can guide and accelerate the ions to have a certain energy, and the surface of materials is etched when the ions bombard on it. According to the Table 3.1 [48] shown below, the reason that dry etching is wildly used for micro-fabrication in modern times can be easily found.

Characteristic	Wet Etching	Dry Etching
Etch Rate	Fast	Slow
Selectivity	High	Moderate
Resolution	Fair	Good
Anisotropic	Difficult	Good
Control	Not easy	Easy
Cost	Low	High
Waste Disposal	High	Low

Table 3.1 Comparison of wet etching and dry etching

There are three types of dry etching operation modes: physical sputtering, plasma etching and reactive ion etching.

Physical sputtering uses a glow discharge to ionize gases such as argon into positively charged ions, then bias voltage can accelerate the ions and push them hitting on the surface of target materials [49]. This process is completely a physical energy transferring process, and it can obtain a nearly vertical sidewall profile with good directional etching. These phenomena can be categorized as an atomic collision [50]. However, the ions hit uniformly the sample surface, and both the etching mask and the material will be etched which results in low selectivity. Therefore, completely physical sputtering method is rarely used in the ultra-large-scale integrated circuits fabrication process.

Plasma etching is the use of plasma to ionize gas to form charged particles, molecules and highly reactive atomic groups, and they diffuse to the surface of the target film. Since it mainly utilizes chemical reactions, the etching process is similar to the wet etching described above except the state of the reactants and products is changed from a liquid state to a gaseous state, and plasma is used to accelerate the reaction rate. Therefore, chemical dry etching has advantages and disadvantages similar to wet etching, and the purely chemical etching method is applied only in processes which does not require pattern transfer in the semiconductor fabrication.

Reactive ion etching is the combination of chemical reaction and ion bombardment, so it has high etching rate and high anisotropy. The etching is mainly carried out by chemical reaction, and the effect of adding ion bombardment is in two aspects. First, it can destroy the chemical bond on the surface of target materials to increase the etching rate. Second, it can attack the passivation materials created by etching process deposited as a film.

As a result, reactive ion etching is the most effective type of dry etching, and a new technique named deep reactive ion etching (Bosch process) is introduced to obtain high aspect ratio structures.

3.3.2.1 Bosch process

Bosch process, also known as deep reactive ion etching (DRIE) or time-multiplexed etching, alternates the etching process and passivation process repeatedly to achieve highly anisotropic structures. In order to ensure the stability and reliability of the passivation layer to fabricate high aspect ratio structures with steep sidewalls, Bosch process separates the deposition of the passivation layer and the etching of the single crystal silicon into two separate steps to avoid the interaction between deposition and etching. Sulfur hexafluoride (SF_6) is used to etch the sidewalls and the bottom of the trenches or holes in the etching step, and octafluorocyclobutane (C_4F_8) is a protective gas used in the passivation step. It is worth mentioning that the passivation layer is a layer of CF_x organic polymer protective film on the sidewall surface, and Figure 3.8 gives the schematic representation of Bosch process.

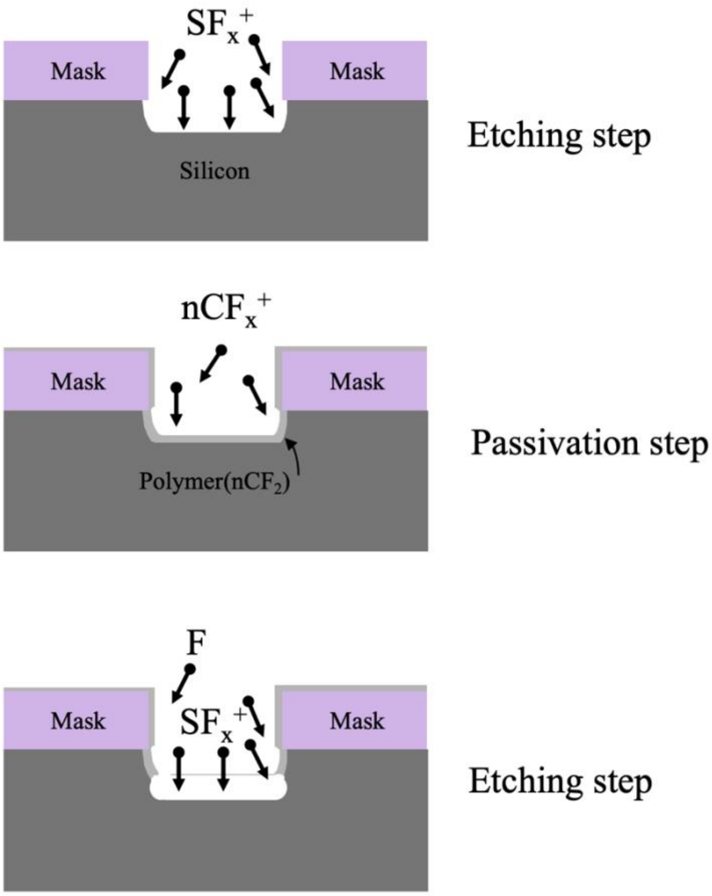

Figure 3.8 Schematic representation of Bosch process

C_4F_8 decomposes into ionic CF_x group under the plasma state, and the CF_x group adsorbs on the silicon surface to form polymer layer $(CF_2)_n$. Then, the polymer passivation film is etched in a new round of etching step with more SF_6 gas introduced to increase the F ion dissociation, and the passivation film is then etched away [49]. This can lead to deeper sidewall with cycles of Bosch process to achieve effective anisotropic etching. The reaction mechanism is followed by a type of dissociation reaction [51]:

$$\mathrm{SF_6 + e^- \rightarrow SF_5^+ + F + 2e^-}$$

where SF_6 is dissociated to SF_{5+} and fluorine atom. The silicon reacts with fluorine, so the etching step is

$$\mathrm{Si + 4F \rightarrow SiF_4}$$

where atomic fluorine and the product SiF_4 are gas phase. The passivation step is

$$\mathrm{C_4F_8 + e^- \rightarrow C_3F_6 + CF_2 + e^-}$$

Then CF_2 group absorbs on the silicon surface to form polymer layer $(CF_2)_n$.

In experiment, the recipe of standard Bosch process is shown below in Table 3.2. In the Bosch etching step, the gas flow of SF_6 is 160 sccm, with ICP power 1000W, RF power 20W, pressure 15 mTorr; and in the Bosch passivation step, the C_4F_8 gas flow is 160 sccm, with ICP power 1000W, RF power 5W, pressure 20 mTorr.

Parameters		Etching step	Passivation step
Pressure (mTorr)		25	20
Temperature (Deg c)		15	15
RF power (W)		20	5
ICP power (W)		1000	1000
Gas out (sccm)	C_4F_8	0	160
	SF_6	160	0
Time (s)		7	5

Table 3.2 The recipe of standard Bosch process

Although Bosch process can create high aspect ratio structures, the profile of sidewall is rough/wavy [52] which is shown in Figure 3.9. This is caused by the different etching rate of the bottom and the sidewall when alternating the etching step and passivation step, and the rate of etching in vertical direction is much faster than that in horizontal direction. In order to improve the undercut and roughness, non-switching pseudo-Bosch process can be applied.

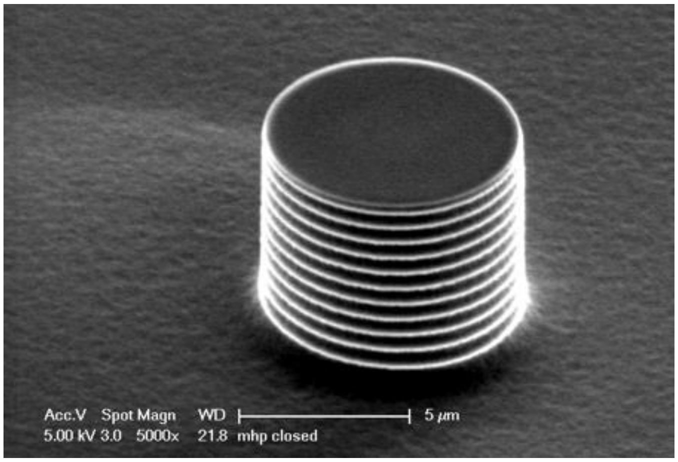

Figure 3.9 The SEM image of sample after Bosch process [52]

3.3.2.2 Cryogenic etching process

Unlike the Bosch process, cryogenic etching (cryo etching, at <~80$_o$C) is a continuous process with SF_6 and O_2 gas in the vacuum chamber simultaneously. Silicon is removed in the form of volatile SiF_4 by reacting with SF_6 gas, and a blocking layer of SiO_xF_y is formed on the sidewall instead of using fluorocarbon passivation layer in Bosch process [53]. Note that SiO_xF_y becomes not volatile at such low temperature, thus acting as a sidewall passivation layer needed for anisotropic etching. With help of cryogenic temperatures, the fluorine radicals are inhibited to attack the blocking layer. It has some advantages such as offering smoother sidewalls and perfect positive profiles over Bosch process, but the limitations of etching rate and cryogenic temperatures are still existing.

3.3.2.3 Non-switching pseudo-Bosch process

Non-switching pseudo-Bosch process is a process similar to Bosch, but here the two gases are used (co-exist) at the same time in the chamber. The first one is SF_6 to etch silicon, and the second one is C_4F_8 to deposit a chemically inert passivation layer. In order to achieve positively tapered tip profile, the gas flow ratio of C_4F_8 and SF_6 can be chosen to adjust the sidewall taper angle, with ICP power 1200 W, RF power 20 W, pressure 10 mTorr. As a result, high aspect ratio nanostructures with smooth sidewall can be fabricated by the non-switching pseudo-Bosch process, so this process is suitable for fabricating HAR tip in AFM system.

Also, the non-switching pseudo-Bosch process can be improved by introducing oxygen plasma cleaning step into it, and the detailed principle is presented in Chapter 4.

3.4 Experiment process and results

Figure 3.10 represents the fabrication steps of HAR silicon AFM tip. All techniques including e-beam evaporation, bilayer photoresist method, e-beam lithography and etching process are used in this work. Here, the detailed information will be discussed.

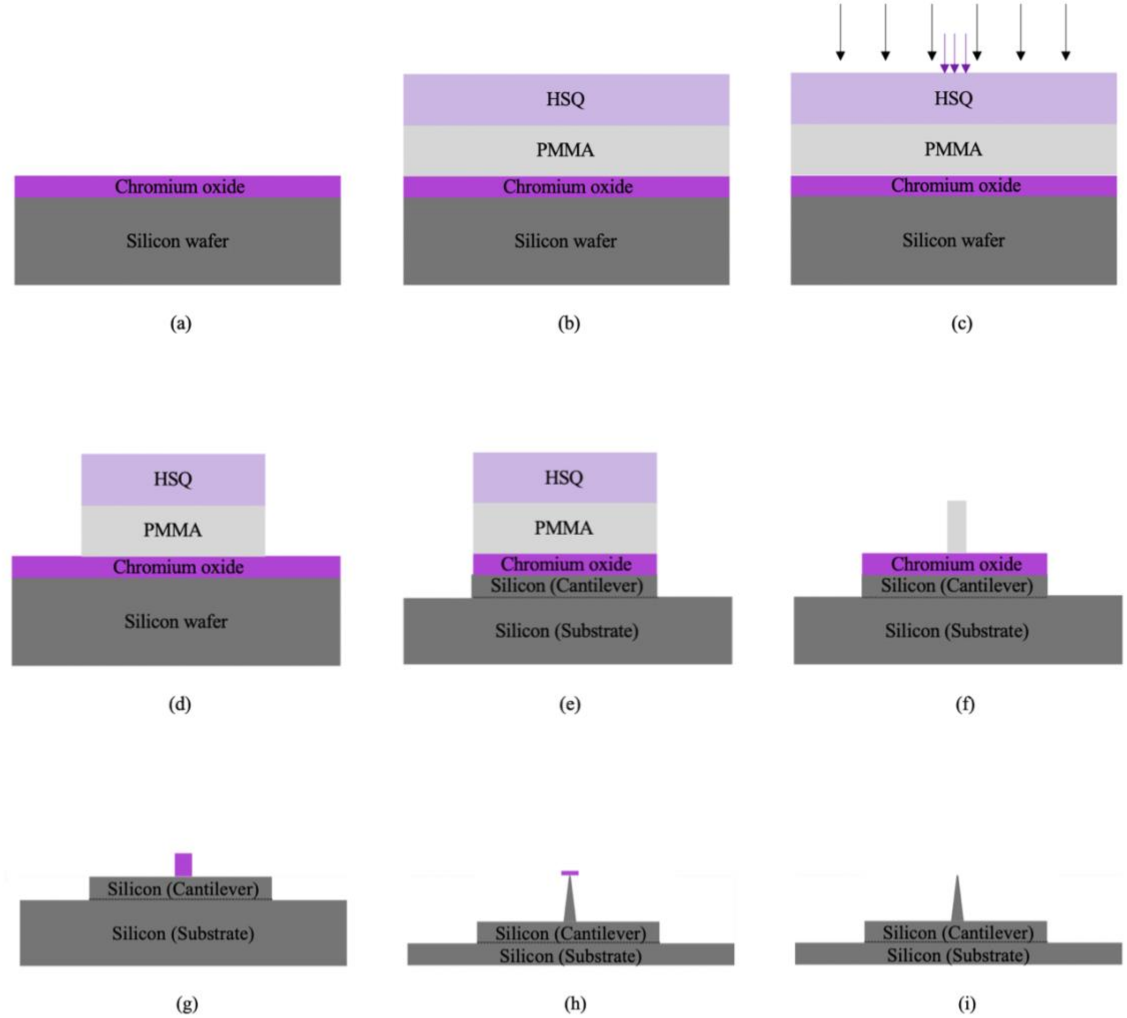

Figure 3.10 The fabrication steps of HAR silicon AFM tip

A silicon wafer is first cleaned with acetone and isopropanol (IPA) rinse, and 2-minite oxygen plasma with 20sccm O_2 gas flow under 20W RF power and 20mTorr chamber pressure conditions. After cleaning process, 150nm Cr_2O_3 is evaporated by Intlvac e-beam evaporator on bare silicon (Figure 3.10a). Cr_2O_3 is suitable to be the hard mask of silicon with high selectivity, and the rate of layer deposition is 0.1nm/s to ensure the uniformity of the mask. Then, the bilayer of e-beam photoresist including PMMA and HSQ is spin-coated on hard mask. The first layer of 500nm PMMA (8% in anisole) is spin-coated at 3000rpm for 50 seconds and baked on hotplate at 180 ℃ for 10 minutes, and the second layer of 500nm HSQ (10% in MIBK) is spin-coated at 2000rpm for 50 seconds and baked on hotplate at 90 ℃ for 5 minutes (Fig 3.10b). Then electron beam lithography using a Raith 150TWO system at 20kV is applied to pattern structures. In order to test the repeatability and reduce risks of broken, we designed 9 tips on one cantilever. Tip pattern is determined by PMMA resist at the dose of 10000 $\mu C/cm^2$ to present negative tone, and cantilever pattern is determined by HSQ resist at the dose of 50 $\mu C/cm^2$ (Fig 3.10c). Note that the PMMA will not be affected by the low dose of 50 $\mu C/cm^2$, and over-exposure of HSQ with a dose of 10000 $\mu C/cm^2$ at the tip pillar site will not damage it, either.

Next, the unexposed area of HSQ resist is removed by AZ300 MIF developer for 1 minute, and HSQ can be the mask to etch PMMA by 30 sec oxygen plasma etching with 20sccm O_2 gas flow under 20W RF power and 20 mTorr chamber pressure conditions (Fig 3.10d), and Cr_2O_3 hard etching mask was obtained by wet etching for 5 minutes. The cantilever pattern is then transferred to the following silicon layer by 8 cycles of standard

Bosch process at a ~400 nm/cycle etching rate (Fig 3.10e). After the fabrication of cantilever part, HSQ can be removed by 1:50 diluted hydrogen fluoride (HF) solution for 60sec. To fabricate tip part, PMMA is first developed by anisole for 3min, and it can be used to be the mask of Cr_2O_3 (Fig 3.10f). After wet etching or metal RIE etching of Cr_2O_3 (Fig 3.10g), 40min non-switching pseudo-Bosch process with gas flow of 60 sccm (42 sccm C_4F_8 + 18 sccm SF_6) is applied to obtain tip structure (Fig 3.10h). After the removal of the remaining Cr_2O_3 layer, the HAR tip on the cantilever is obtained finally.

The SEM image of final structures of tip and cantilever is shown below in Figure 3.11. The block in front of the tips can be used as a mark which was exposed at the dose of 3000 $\mu C/cm_2$, and it also can indicate the overall height of silicon that I etched away. The average height of tips is around 5 μm, and the average diameter of tip apex and tip base is 18.5 nm and 785.2 nm, respectively. The height of the cantilever part is about 3 μm.

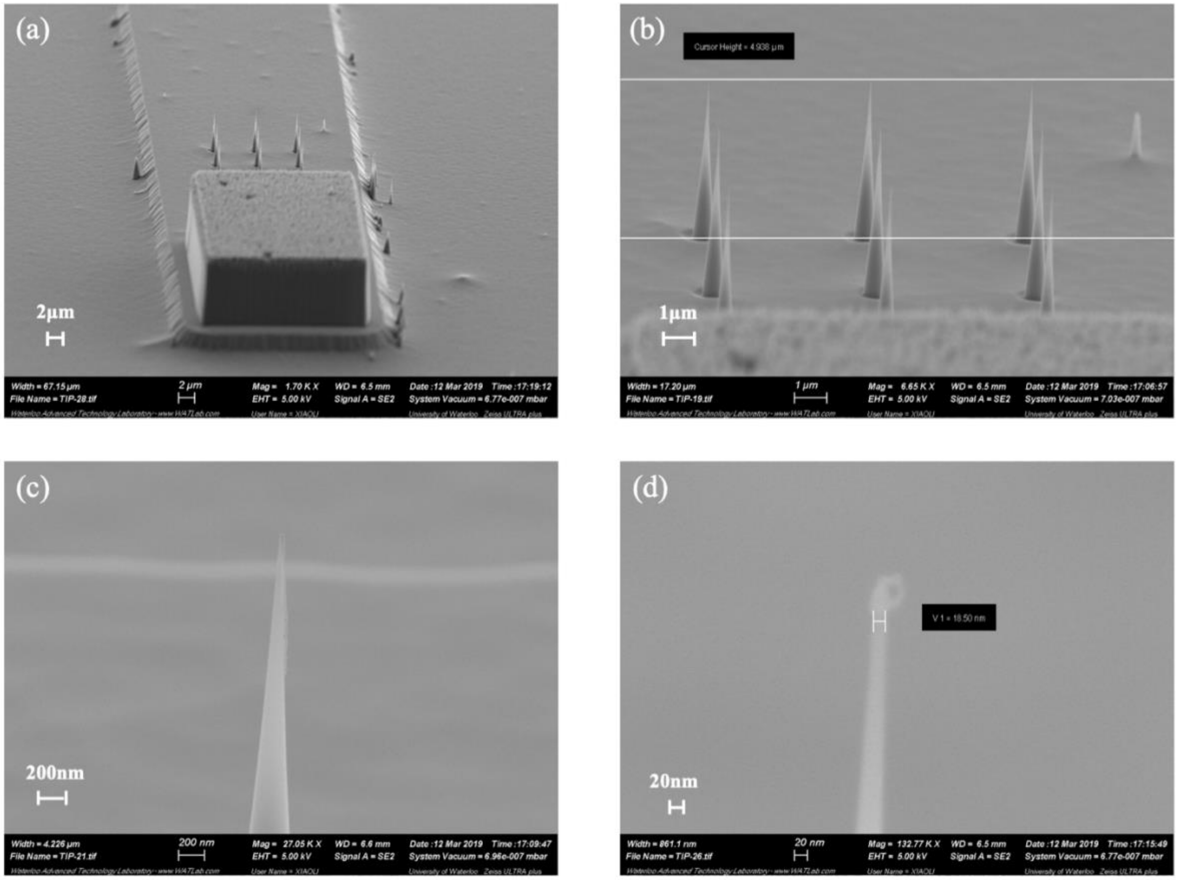

Figure 3.11 The SEM images of final HAR AFM tips

According to the fabrication result and SEM images, the diameter of tip apex can reach to 18.5nm. Figure 3.12 gives the measurement data of Figure 3.11 (c), and it shows an aspect ratio better than 6 (exact value is 6.098) at a tip height of 1 μm. Due to the sharpness of tip apex and aspect ratio, these tips can be considered as pretty good high aspect ratio AFM tips, and this process is suitable for achieving the fabrication of HAR AFM tip part.

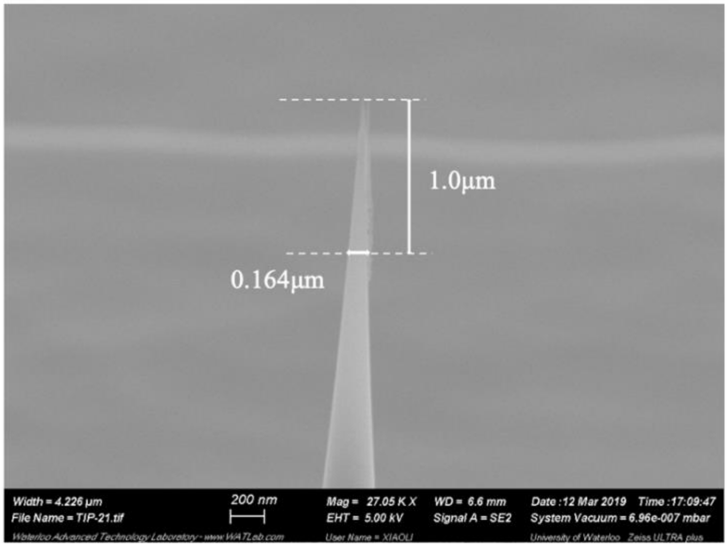

Figure 3.12 The measurements of aspect ratio on tip apex. The scale bar is 200 nm.

However, the fabrication process can still be improved to obtain better tip profile, and oxidation sharpening would be the most effective ways to achieve it. After that, oxygen plasma cleaning after fabrication can remove the contamination residue on tips to make the profile better.

Here we covered only the fabrication of the front side of a complete AFM probe. For patterning the tip handle part, backside patterning using deep silicon etching would be needed to etch through the wafer to reach the isolation layer (the oxide layer) of a SOI wafer. At present, the backside handle fabrication is being carried out by other group members.

3.5 Summary

In this chapter, a method to fabricate HAR AFM tips by EBL on the bilayer of electron beam resist and RIE is introduced to tackle the issue of low throughput and high cost of other HAR tip fabrication process. Different doses were applied to PMMA and HSQ resist in EBL, and tip pattern and cantilever pattern were transferred to silicon by dry etching. In the experiment, the diameter of tip apex can reach to 18.5nm, and the aspect ratio is better than 6 at a tip height of 1 μm. This method is suitable for achieving the fabrication of HAR AFM tip part. The fabrication of tip handle part will be carried out later on using deep silicon etching.

Chapter 4 Effect of oxygen plasma cleaning on non-switching pseudo-Bosch etching of high aspect ratio silicon pillars

This chapter is related to non-switching pseudo-Bosch etching process. Here we present an improved method by introducing oxygen plasma cleaning step, and this work is published in Journal of Vacuum Science & Technology B [54]. I would like to express my gratitude to Dr. Ferhat Aydinoglu, he provided many ideas of adding oxygen plasma with different recipe and helped me to prepare the samples. I would also like to thank my colleague Chenxu Zhu, he finished the additional testing of etching rate and helped me a lot with analysis of results.

4.1 Introduction and motivations

Dry etching of silicon is widely used in nanostructure fabrication, as it works better than wet etching due to high anisotropy and selectivity [55]. The long-term goal of dry etching is to have high etching rate, high etching selectivity to mask material, vertical or controllable sidewall profile, and smooth sidewall, so non-switching pseudo-Bosch recipe was introduced to this area since standard Bosch process leads to wavy/rough sidewall profile by switching between SF_6 and C_4F_8 gas [56][57][58]. In the process, SF_6 and C_4F_8 gases are existed simultaneously to obtain nanostructures with smooth sidewall profile instead of switching the etching step and passivation step. It is reported that the sidewall taper angle is tailored over a broad range from zero degree to forty degree when different ratio of SF_6 and C_4F_8 gases mixture are introducing to the chamber [58].

However, one of the challenges in non-switching pseudo-Bosch process is the formation of contaminations such as excess passivation residues and silicon fragments produced during the process that will influence the etching rate and profile of structures [40]. The problem of passivation residues also exists in standard Bosch process. To overcome the problem, many attempts have been made. Some authors added a third individual step which is called depassivation step by introducing argon (Ar) and/or O_2 gas into the chamber after the passivation step [59][60][61] since O_2 and Ar plasmas are two usual mechanisms for depassivation step in standard Bosch process which do not chemically react with Si. Although Ar plasma can remove the passivation polymer residue by physical sputtering, the argon plasma is very directional that helps removal of passivation polymer at the base faster than the sidewalls which will lead to redeposition of the polymer on the sidewalls that results in a non-uniform etching. O_2 plasma can remove the fluorocarbon polymer chemically at horizontal surface, and the etch product is volatile. Here we show that, by introducing periodic O_2 plasma cleaning step, that is, switching between SF_6/C_4F_8 etching and O_2 cleaning, the etching rate can be significantly improved, without any adverse effect.

Similar to the depassivation step in standard Bosch process, we divided non-switching pseudo-Bosch process into many discontinuous steps/cycles, with cleaning steps using oxygen plasma inserted in-between these etching steps. Oxygen plasma is preferred to effectively remove the contaminations without significant attack of silicon and chromium mask.

4.2 Experiment

In the experiment, E-beam lithography and lift-off was performed to form the Cr hard mask, and oxford Instrument PlasmaLab100 ICP 380 was employed for the etching study. Silicon was etched by alternating SF_6/C_4F_8 and O_2 plasma, rather than adding O_2 gas into SF_6/C_4F_8 gas mixture. That is, the process is a switching one. Below Table 4.1 shows the etching and O_2 plasma cleaning recipe.

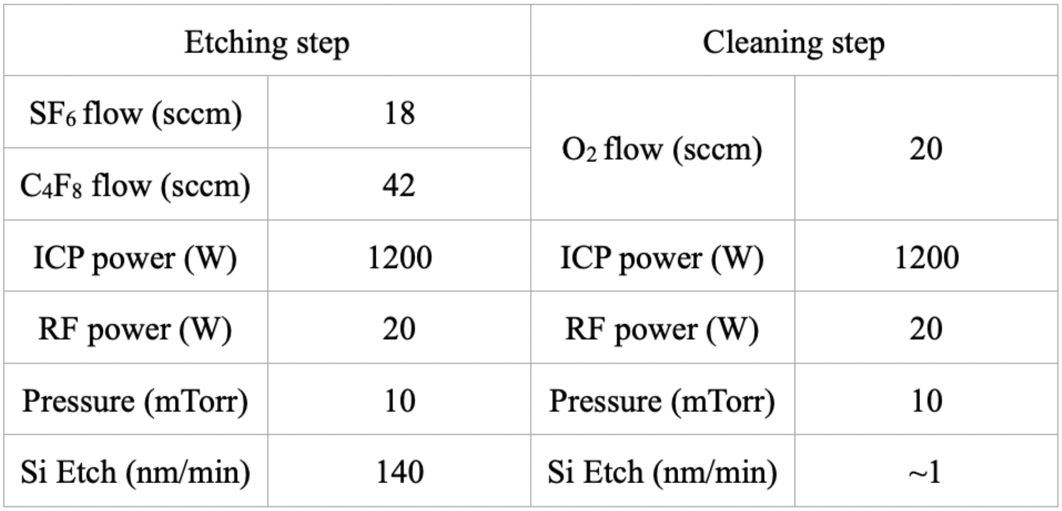

Etching step		Cleaning step	
SF_6 flow (sccm)	18	O_2 flow (sccm)	20
C_4F_8 flow (sccm)	42		
ICP power (W)	1200	ICP power (W)	1200
RF power (W)	20	RF power (W)	20
Pressure (mTorr)	10	Pressure (mTorr)	10
Si Etch (nm/min)	140	Si Etch (nm/min)	~1

Table 4.1 The recipe of etching step and cleaning step

Thirteen samples with different conditions to evaluate the effect of periodic oxygen plasma cleaning are shown in Table 4.2. All samples were first cleaned with 60 sec oxygen plasma before the Si etching started and cleaned again after the end of the Si etching. In the etching step, the total etching time was kept constant at 2400 sec; total gas flow of 60 sccm (42 sccm C_4F_8 + 18 sccm SF_6), 1200 W ICP power, 20 W RF power and 10 mTorr pressure at 15 °C were maintained for all samples. In the depassivation step, the O_2 gas flow is 20 sccm, with ICP power 1200 W, RF power 20 W, pressure 10 mTorr, and temperature 15 °C.

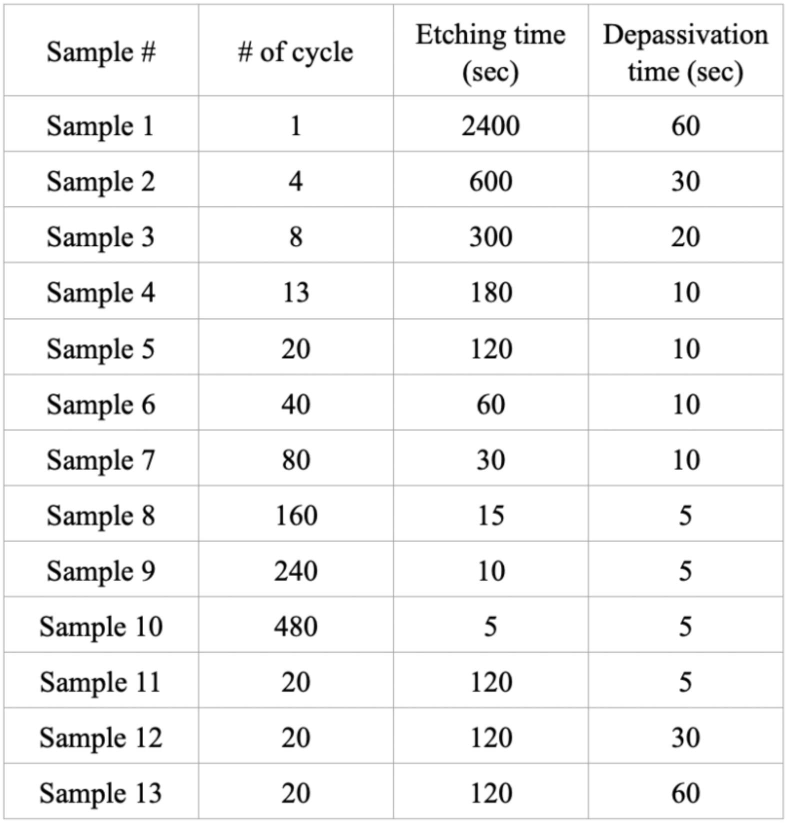

Sample #	# of cycle	Etching time (sec)	Depassivation time (sec)
Sample 1	1	2400	60
Sample 2	4	600	30
Sample 3	8	300	20
Sample 4	13	180	10
Sample 5	20	120	10
Sample 6	40	60	10
Sample 7	80	30	10
Sample 8	160	15	5
Sample 9	240	10	5
Sample 10	480	5	5
Sample 11	20	120	5
Sample 12	20	120	30
Sample 13	20	120	60

Table 4.2 Summary of varied etching parameters

As mentioned before, etching taper angle can be controlled by tuning the gas flow ratio. Since the gas flow ratio of $SF_6/C_4F_8 = 18/42$ was selected, the etched pillar has a slightly positively tapered sidewall profile (the ratio of 22/38 will lead to vertical profile as shown in previous study [58]). The reason for choosing the gas flow ratio of 18/42 with a higher flow of C_4F_8 is to observe the effect of the O_2 plasma cleaning more obviously. On the other hand, too much C_4F_8 slows the etching significantly that would make the pillar height differences less apparent.

4.3 Results and discussion

The detailed information of etched pillars is shown in Table 4.3.

Sample #	# of cycle	Pillar height (µm)	Pillar diameter (µm)	Etching rate (nm/min)	Aspect ratio
Sample 1	1	5.57	1.09	139	1:5.1
Sample 2	4	7.24	1.38	172	1:5.2
Sample 3	8	8.35	1.21	196	1:6.9
Sample 4	13	8.88	1.41	216	1:6.2
Sample 5	20	8.49	1.12	196	1:7.4
Sample 6	40	9.77	1.28	209	1:7.5
Sample 7	80	6.69	1.1	125	1:5.9
Sample 8	160	4.55	-	85	-
Sample 9	240	2.97	-	-	-
Sample 10	480	-	-	-	-
Sample 11	20	7.75	1.27	186	1:6.1
Sample 12	20	9.68	1.33	194	1:7.3
Sample 13	20	2.42	1.63	40	-

Table 4.3 Summary of etching results

*The pillar diameter is the average diameter of pillar top and base; the etching rate is the etched height divided by the sum of etching and depassivation time.

Sample 1 is the control group to be the comparison with other samples, and it is obtained by 1 cycle of 40min etching step without the depassivation step. The overall etching step with etching rate of 139 nm/min results in a pillar with 5.57 μm height and 1:5.1 aspect ratio. For sample 2, there are 4 cycles of switching 600 sec etching step and 30 sec depassivation step, so the etching/depassivation time ratio is 20. Sample 3 is similar to sample 2 with 8 cycles of switching 300 sec etching step and 20 sec depassivation step, so the etching/depassivation time ratio is 15. The SEM images of sample 1, 2 and 3 are shown in Figure 4.1.

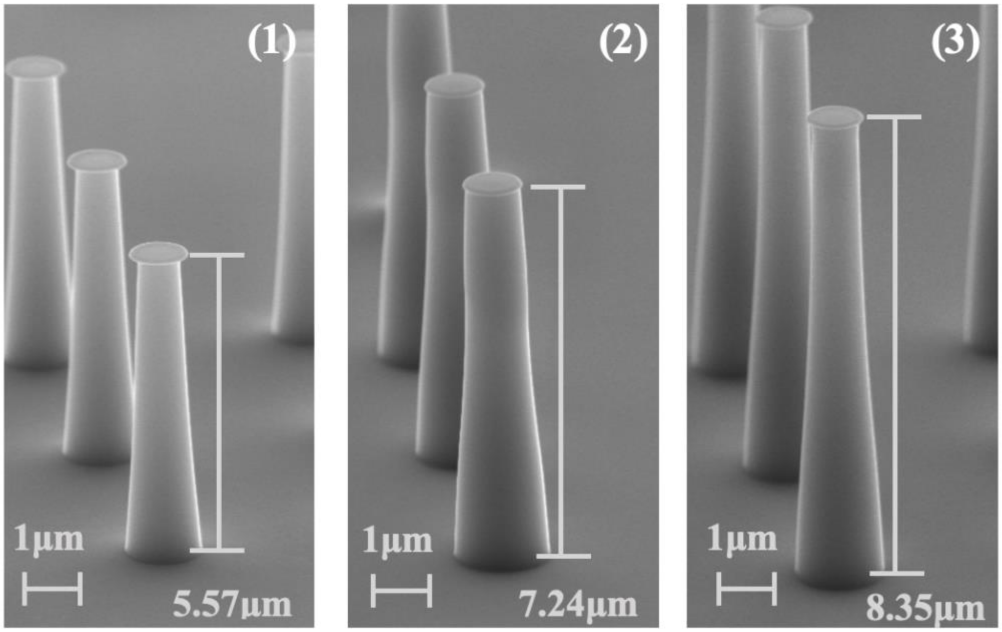

Figure 4.1 SEM images of sample 1, 2 and 3

*The heights are indicated in images, and the Cr hard mask was not removed. All scale bars are 1 μm.

The results indicate that the etching rates of sample 2 with addition of 4 cycles of depassivation step and sample 3 with 8 cycles are 172 nm/min and 196 nm/min, and the aspect ratio is 1:5.1 and 1:5.2, respectively. It is obvious that more cycles of depassivation step inserting to the etching step boosted the etching rate, and the aspect ratio is slightly improved when the total etching time was maintained at 40 min all the time.

For the following conditions of sample 4 to 7, the depassivation duration was kept constant at 10 sec/cycle, and the total etching time was also 40 min. There are 13, 20, 40, 80 cycles of switching etching step and 10 sec depassivation step for sample 1, 2, 3, 4, so the etching/depassivation time ratio is 18, 12, 6, and 3, respectively. The SEM images of sample 4 to 7 are shown in Figure 4.2.

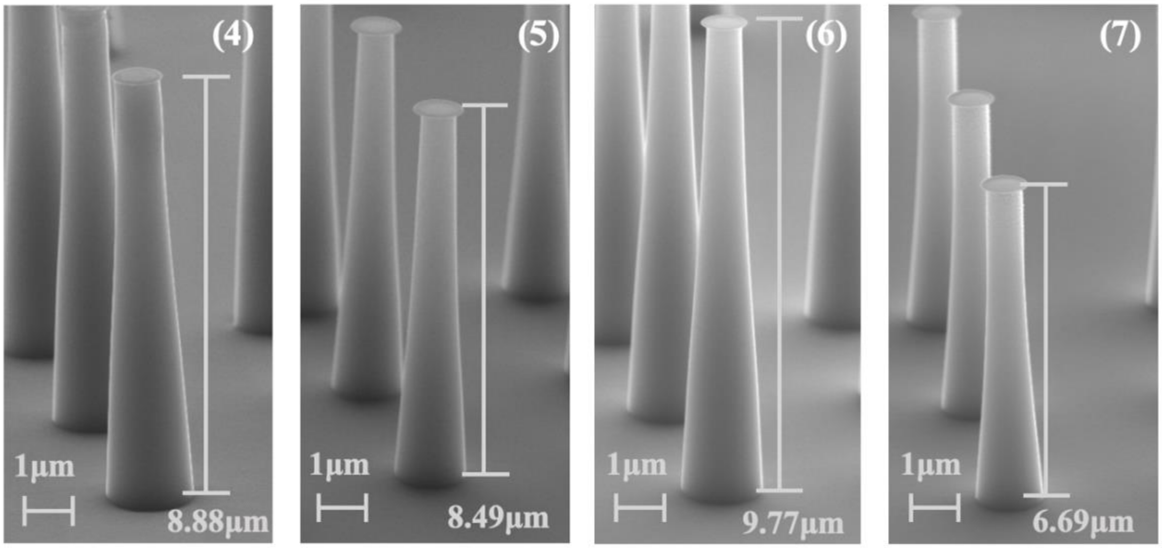

Figure 4.2 SEM images of sample 4, 5, 6 and 7

*The heights are indicated in images, and the Cr hard mask was not removed. All scale bars are 1 μm.

The results indicate that the etching rates of sample 4 with addition of 13 cycles of 10 sec depassivation step, sample 5 with 20 cycles, sample 6 with 40 cycles and sample 7 with 80 cycles are 216, 196, 209, 125 nm/min, and the aspect ratio is 1 over 6.9, 6.2, 7.4, 7.5, respectively. Comparing with sample 1, increasing depassivation frequency increased the etching rate from sample 1 to sample 4, and sample 6. Although the same trend was expected for sample 5, it showed slower etching rate. The reason could be that the factors such as chamber and wafer temperature, chamber contamination condition for every round etching in dry etching process are slightly different [62]. Further increase of the cleaning time in sample 7 reduces the etching rate, likely due to the formation of the hard-to-etch SiO_2. When the excess depassivation step/oxygen time is introducing into the chamber, the top few nanometers silicon of sample will be oxidized, and the selectivity between Cr and Si is much higher than that between Cr and SiO_2. Then the etching rate is obviously decreased in surface oxidation condition.

When the cycles are increasing to 160, 240 and 480 for following samples from 8 to 10, the depassivation duration was maintained at 5 sec/cycle, and the total etching time was also 40 min. The SEM images of sample 8 to 10 are shown in Figure 4.3.

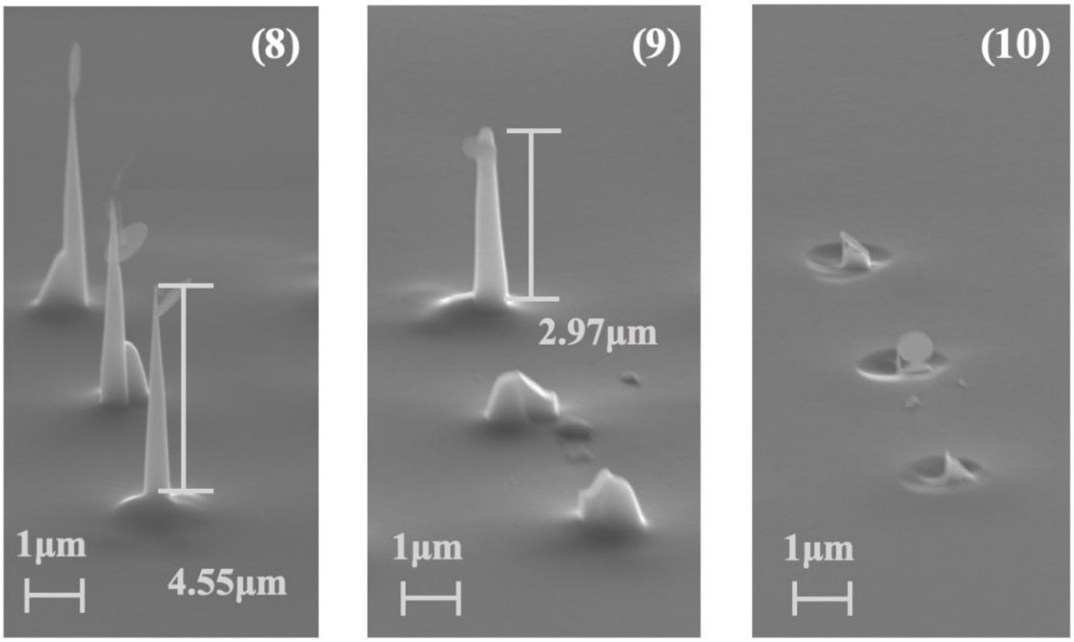

Figure 4.3 SEM images of sample 8, 9 and 10

*The heights are indicated in images, and the Cr hard mask was not removed. All scale bars are 1 µm.

As mentioned before, the results show that more frequent cleaning gave higher etching rate and aspect ratio from sample 1 to 4 and sample 6. However, too frequent cleaning led to worse result, such as lower etching rate likely due to excess surface oxidation by oxygen plasma knowing that oxide is harder to etch than silicon (sample 7), and too much lateral etching causing mask falling off likely due to the excess removal of sidewall passivation layer (sample 8 to 10).

As a result, sample 6 with fixing total etching time divided to different cycles has the highest etching rate with the highest pillar height of 9.77 µm and the aspect ratio of 1:7.5, and this result is obtained by 40 cycles of 60 sec etching and 10 sec cleaning. In order to figure out the effect of the time of depassivation step itself to the etching rate and aspect ratio, conditions of same cycles of depassivation step with different oxygen plasma time inserting into identical cycles of etching step were also applied to sample 11-13. Here we fixed the etching time as 120 sec (same as the previous sample 5), and varied the cleaning time from 5 to 60 sec.

The SEM images of sample 11 to 13 and sample 5 are shown in Figure 4.4.

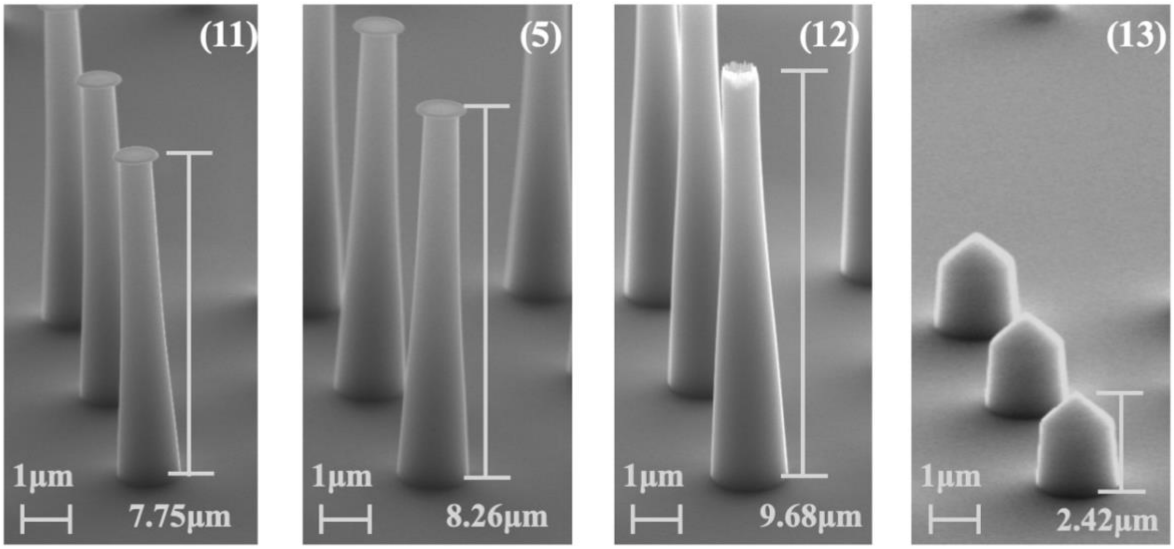

Figure 4.4 SEM images of sample 11, 5, 12 and 13.

*The heights are indicated in images, and the Cr hard mask was not removed. All scale bars are 1 μm

The results show that longer cleaning time per cycle boosted the etching rate and aspect ratio when the total cycle is fixed, but not dramatically, so we consider 10-20 sec as suitable cleaning time. However, too long cleaning time leads to serious mask erosion (sample 12 and 13). Apparently, the fluorocarbon polymer residue on horizontal surface is not mono layer covering on surface. Otherwise, it would be sufficient to remove the residue with several sec cleaning step, as one would imagine needed for continuous silicon etching. It was reported that free radicals like fluorine (F) can penetrate around 5 nm of fluorocarbon polymer underneath to etch the silicon [63]. Another possible mechanism is that O_2 plasma may render the top Si surface amorphous by ion bombardment, and it becomes easier to etch, but this will not play a significant role since the amount of Si etched during each cycle is far beyond the amorphous Si layer thickness.

4.4 Summary

It was showed that the method of switching between SF_6/C_4F_8 etching and O_2 cleaning by introducing periodic O_2 plasma cleaning step can significantly improve the etching rate without any adverse effect. In this experiment, a cleaning step of order 10 sec is considered as optimal finally. Too long cleaning step leads to slower etching rate due to hard-to-etch SiO_2 formation, serious mask erosion and lateral/undercut etching.

Chapter 5 Fabrication of ultra-high aspect ratio silicon nanopillar arrays

This chapter covers a new method using DRIE and wet etch sharpening to fabricate ultra-high aspect ratio silicon nanopillar arrays. The results show that the aspect ratio can be up to approximately 130.

5.1 Introduction to HAR nanopillars

High aspect ratio structures have potential applications in fields including high aspect ratio tip and micro/nano needles for clinical use. The first application, high aspect ratio AFM tip, can give higher resolution and clearer restoration in the imaging process. The cost of the conventional standard fabrication process by introducing different combinations of processing technology including deposition, lithography and etching is pretty high. The background and detailed information of HAR AFM tip are covered in Chapter 3, thus only nanoneedles will be introduced in this part.

The hypodermic needle became widely used in clinical and forensic settings in the late 19th century [64]. The appropriate needle gauge of the most widely used as hypodermic needles in recent years is 25G, which means the outer diameter is 0.5 millimeters. However, patients are observed to resist conventional needles due to pain and anxiety [65]; microneedle technologies came into our views in the past decade. Usually, transdermal drug injection or fluid extraction only requires very small holes, so the diameter of the needle tip can be reduced to several tens micrometers to minimize pain and prevent skin and tissue damage. Previous studies reported that microneedles with various tip diameters ranging from 10 to 50μm [66] can smoothly penetrate into skin in clinical use, and the tip radii can reach to 5μm to perform good penetrability and sufficient delivery [69]. Microneedles can be fabricated as hollow structure to inject drugs or extract body fluid for bio-detection.

When the tip diameter decreases to sub-μm scale, it can be used to penetrate cell membrane in molecular delivery. The delivery of substances into cells provides an efficient approach to observe cell behavior and analyze its conditions. In conventional research, scientist tried to use liposomes [67] and viral vectors [68] to send the target functional biomolecules, DNAs or RNAs, into cells or tissue organs to obtain the functional product for the treatment of various diseases, but challenges including poor operability, low efficiency and biological toxicity lead to unsatisfying results. Also, it was reported that protein transduction domain (PTD) [69] and cell-penetrating peptides (CPP) [70] technologies have been successfully applied to deliver biomolecules, but they are not widely used in clinical treatment due to the complexity of transduction mechanism. In general, it is very difficult to achieve molecular delivery, as the restriction of membrane permeability and structural flexibility will prevent exogenous bioactive substances to perform therapeutic effects [71]. That has led to the development of more direct and physical methods to transfer biomaterials or probe and study the cell behavior, such as those using nano-needles.

High aspect ratio and nanoscale width are two fundamental requirements of nanopillars. Different manufacturing techniques were developed alongside the strategies embraced by the semiconductor industry to promote the development of application-specific nanopillars. Vapor-liquid-solid (VLS) silicon growth is developed and widely used in vertically aligned nanowires synthesis [72], and it can also fabricate nanopillars. In the synthesis of VLS, silicon is integrated into a fluid eutectic Au-Si nanodroplet from the vapor phase precursor, and then silicon will nucleate into solid phase when the concentration exceeds saturation for the eutectic. The growth of nanopillar is strictly controlled by the growth temperature and equilibrium vapor pressure of catalyst [73], so the quality of nanopillars and throughput cannot be guaranteed by using this method.

Metal-assisted chemical etch (MACE) for nanopillar fabrication also requires metal particles or patterns. Here metal nanostructures formed on top of silicon catalyzes nanopillars etching in a mixture of hydrogen peroxide solution and hydrofluoric acid (oxidizing HF solution). Although low cost and large area capabilities are really attractive, this method is not suitable for nanopillar technologies due to complicated etching parameters and uncontrollable quality of products [74].

Since atomic force microscope (AFM) was invented by Gerd Binnig of the IBM Research Center in 1986 [3], significant experimental effort has gone into imaging and analyzing live biomolecules and biomaterials. The tip should not destroy the cell during measurements. The sharpened silicon pyramidal AFM tips have been successfully employed to transfer GFP-encoding plasmid DNA into single primary cultured human mesenchymal stem cells [75]. Two methods are often used to sharpen AFM tips: oxidization and buffered hydrofluoric acid etching [76][51], and focused ion beam milling [77]. The latter method has high cost in production.

This Chapter presents a combined method to fabricate high aspect ratio nanopillar arrays by reactive ion etching and then sharpening to nanoscale by wet etching process. Compared to other methods as we mentioned above, this method would offer both high cell viability and high fabrication throughput. Here, we demonstrate that our nanopillars can achieve ultra-high aspect ratio of order 100.

5.2 Experiment

The schematic of high aspect ratio nanopillar array fabrication process is shown in Figure 5.1. RCA cleaning process was performed on a silicon wafer with <100> surface orientation to remove the ionic and organic contaminations and the natural oxide layer. RCA 1 is a solution of hydrogen peroxide, ammonium hydroxide and deionized (DI) water, and RCA 2 is a solution of hydrofluoric acid, hydrogen chloride, and DI water. Then bilayer of positive tone resist including 250 nm ZEP-520A and 220 nm PMMA resists was spin-coated on the bare silicon wafer, and pre-baked for 3 min at 180 C°. Electron beam lithography using Raith at 20 kV with dose of 500 μC/cm2 was performed to define many 2x4 circular dot arrays with 1 μm diameter (Figure 5.1b), and both electron beam resists were developed with xylene for 2 minutes. According to the different dissolution rates of ZEP and PMMA in the developer, it can create an overhang resist pattern which is favorable for lift-off process (Figure 5.1c).

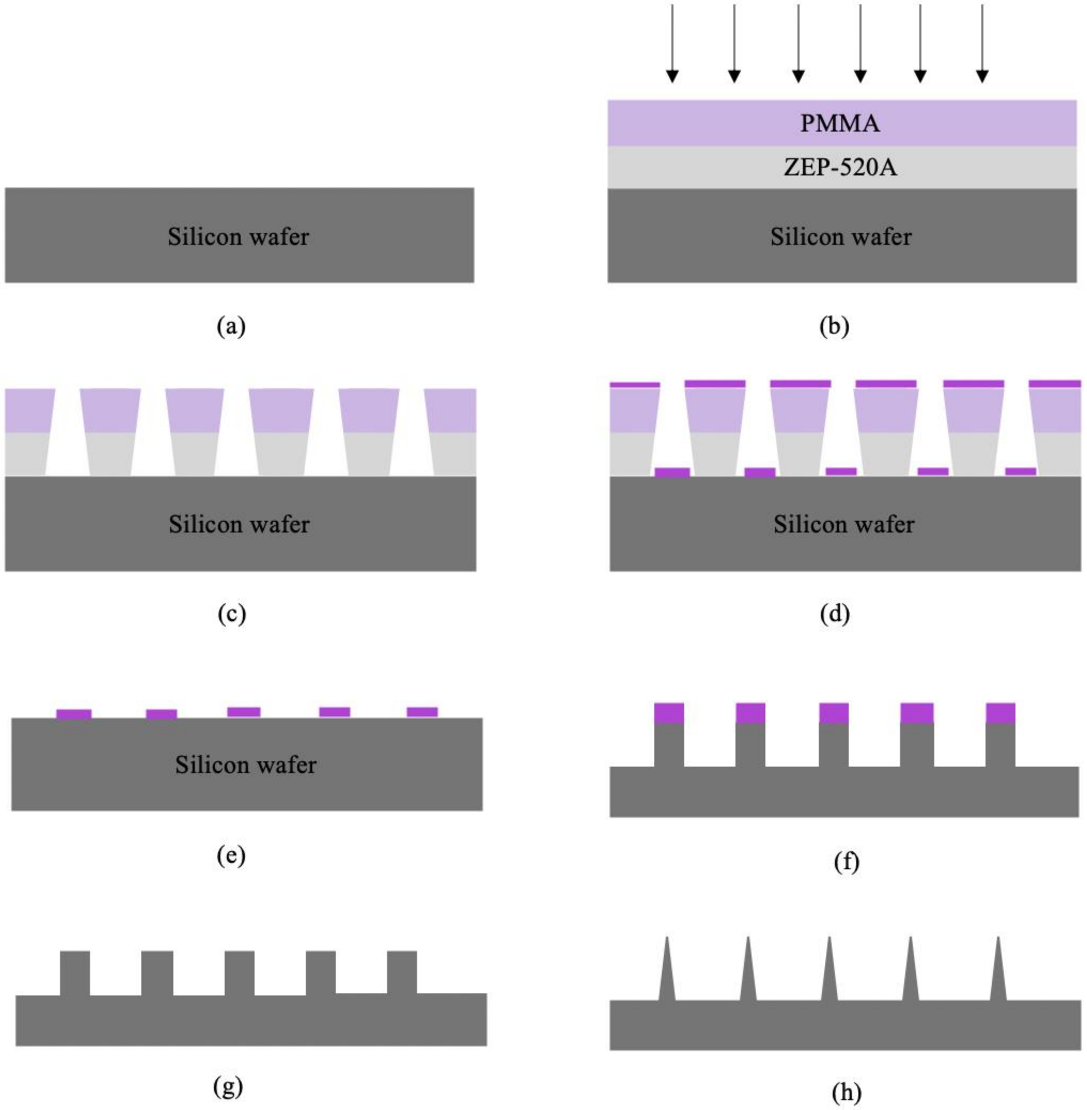

Figure 5.1 Schematic of fabrication and sharpening process for high aspect ratio nanopillar array

After development, 150nm Cr is evaporated by Intlvac e-beam evaporator (Figure 5.1d), and liftoff process is followed by acetone bath with ultrasonic agitation (Figure 5.1e). Then non-switching pseudo-Bosch process was carried out to obtain silicon pillar arrays

(Figure 5.1f). In the etching process, 22 sccm SF_6 and 38 sccm C_4F_8 gases were introduced to the chamber simultaneously, and 1200 W ICP power, 20 W RF power, 10 mTorr pressure at 15 °C were applied in the Oxford ICP380 instrument. After the chromium mask was removed from the top (Figure 5.1g) of nanopillar array having 10μm height, sharpening/thinning down process was conducted by wet etching (Figure 5.1h). Hydrofluoric acid (HF) solution was diluted for more accurate volume measurement (as the HF concentration is extremely low in the final etchant), and then mixed with undiluted nitric acid (HNO_3) solution to obtain a final ratio of HF : HNO_3 = 1 : 200. Note that, since the amount of HF is very low, the water used to dilute it initially can be ignored when calculating the mixing ratio. Finally, the sample was put into the mixture for 8 minutes to sharpen/thin down the nanopillars.

5.3 Results and discussion

After liftoff to fabricate the Cr mask, the silicon plasma etching was carried out to obtain nanopillar arrays, which are shown in Figure 5.2 (a)(b). The measured diameters of top, middle, and bottom part of unsharpened nanopillar are respectively 755nm, 820nm, and 755nm, which shows the pillar profile is nearly vertical. A key point in the fabrication is the non-switching pseudo-Bosch process. In this process, SF_6 and C_4F_8 gases are introduced to the chamber simultaneously, and the gas flow ratio will influence the taper angle of silicon nanopillar sidewall. Our study previously showed that flow ratio of 22/38 leads to vertical profile [58], so it is chosen to etch nanopillars in this experiment.

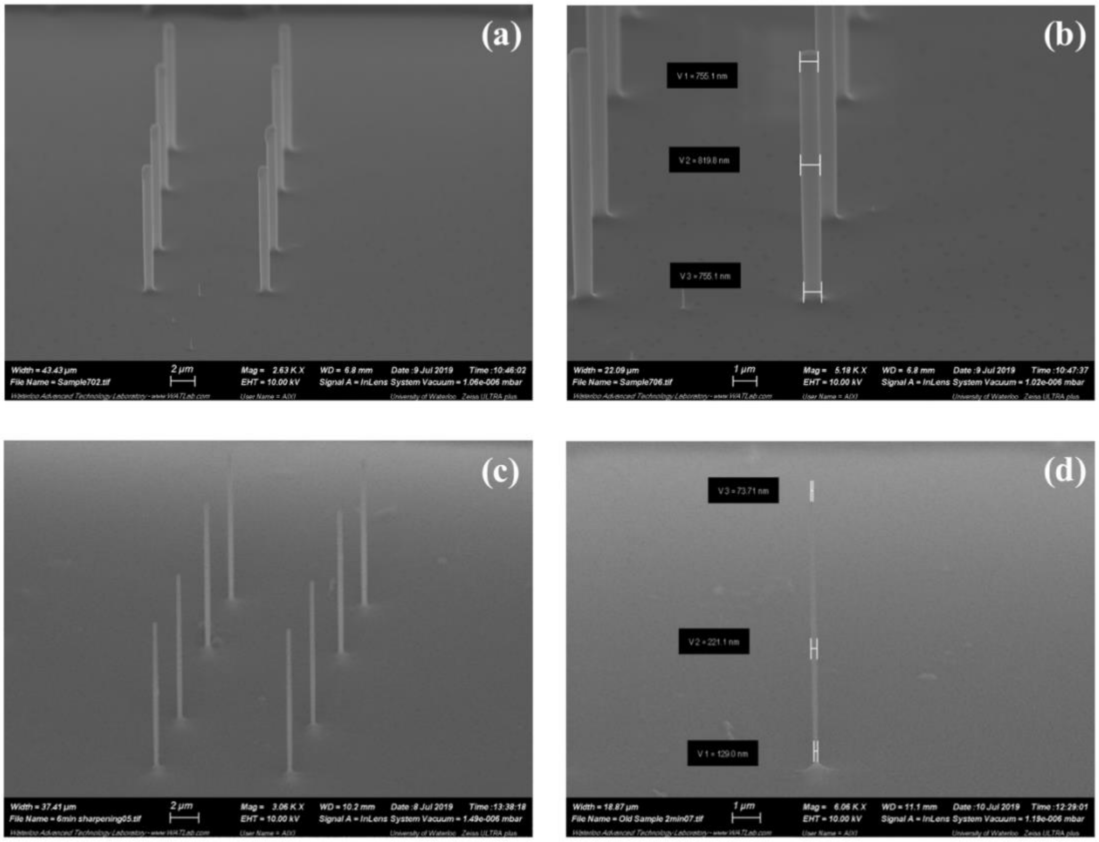

Figure 5.2 (a) Nanopillar array before sharpening process. (b) Detailed information and profile of pillars before sharpening. The diameter of pillar top part is 755nm. (c) Nanopillar array after sharpening process. (d) Detailed information and profile of pillars after sharpening. The diameter of pillar top part is 74nm.

In order to achieve needle-like structure by using isotropic wet etching, chemical system including HNO_3, HF and CH_3COOH/H_2O is applied here to sharpen/thin down the pillars. According to Figure 5.3, the etching rate varies with different weight percentage of HF, HNO_3 and diluent. The oxidation step is rate limiting in the high hydrofluoric acid region, and the oxide removal step is rate limiting in the high nitric acid region [78]. When the ratio of HF/HNO_3 is around 4.5, the silicon etching rate is fastest, and it is determined by the flow of reagent to the surface by diffusion [79].

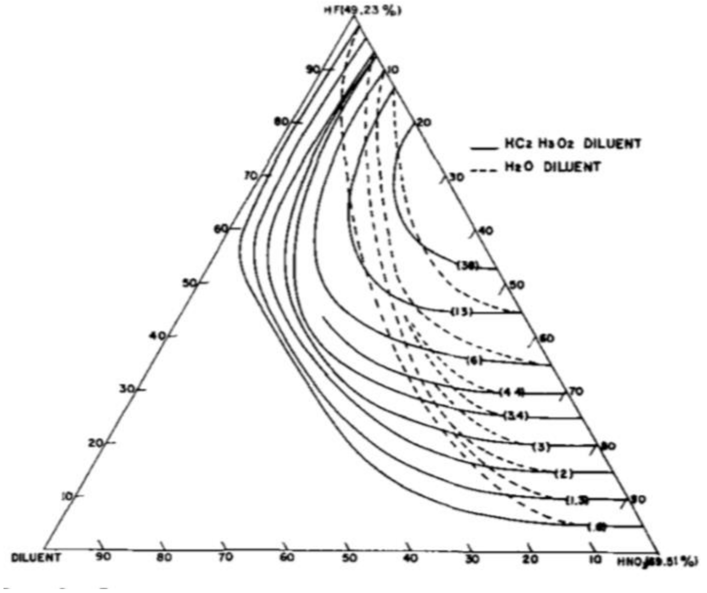

Figure 5.3 Curves of constant rate as a function of etchant composition in the system 49% HF, 70% HNO_3 and diluent (adopted with permission from Ref. [79]).

The addition of H_2O mainly reduces the concentration of HNO_3, thereby reducing the oxidation of silicon. The addition of CH_3COOH with a relatively high dielectric constant reduces the dissolution/decomposition of HNO_3, and it also reduces the oxidation. From Figure 5.3, the reaction rate with CH_3COOH diluent is faster than that with H_2O. When increasing the concentration of diluent from 0% to 10%, silicon structures will be etched away more rapidly with acetic acid diluent than with H_2O diluent, and the sidewall profile is smoother for H_2O diluent [80]. And in the system with H_2O diluent, the sharpening is more effective when the etching step (oxide removal step) is rate limiting in the high nitric acid region.

The etching rate should be slow enough for precise process control in our pillar fabrication due to its nanoscale size, and so a ratio of 200:1 between HNO_3 and HF was chosen in this work. One would be able to obtain similar results if using a different ratio such as HNO_3/HF = 100:1 but adding some water as diluent. In principle, one can also obtain similar low etching rate using a high ratio of HF:HNO_3 (i.e. HF-rich), but the etched surface would be quite rough. In fact, the oxidation of Si is catalyzed by HNO_2 that is always available in nitric acid as an impurity; and when Si is etched, HNO_2 is generated, which in-turn boost further the local Si etching rate. That is, the etching is auto-catalyzed, and when the concentration of nitric acid is low compared to HF concentration, the local etching rate would depend heavily on the initial random availability of HNO_2 impurity at the etching site, leading to rough surface.

After sharpening, the profile is shown in Figure 5.2 (c)(d), and the measured diameters of top, middle, and bottom part of sharpened nanopillar are respectively 74 nm, 221 nm, and 129 nm. As a result, the shrinkage of pillar top part is 681 nm, and that of bottom part is 626 nm.

5.4 Summary

In this chapter, a method to fabricate HAR silicon nanopillar arrays by ICP-RIE and wet-etch sharpening is introduced to overcome the drawbacks of low throughput and high cost of other conventional nanopillar fabrication techniques. Electron beam lithography and lift-off of metal mask was performed for forming array patterns, then ICP-RIE and sharpening was carried out. The pillar apex diameter is 74 nm when the pillar height is 10 μm, so the aspect ratio is very high, approximately 130. As such, ultra-high aspect ratio silicon nanopillar arrays can be achieved using this cost-effective method.

Chapter 6 Conclusions and future direction

All the current commercially available fabrication methods of HAR AFM tips are made one by one which leads to very high price compared to the regular pyramid-shaped tips. To reduce the cost and increase the throughput of HAR AFM tips, we have focused on the fabrication and developing a method to fabricate tips in a batch process. Similar to high aspect ratio tips, high aspect ratio silicon nanopillar array is also widely used. We also present a cost-effective method by using DRIE and wet etch sharpening to fabricate ultra-high aspect ratio silicon nanopillars array. Dry etching in an essential process in micro/nano fabrication techniques, and non-switching pseudo-Bosch etching process can be improved by introducing oxygen plasma cleaning steps.

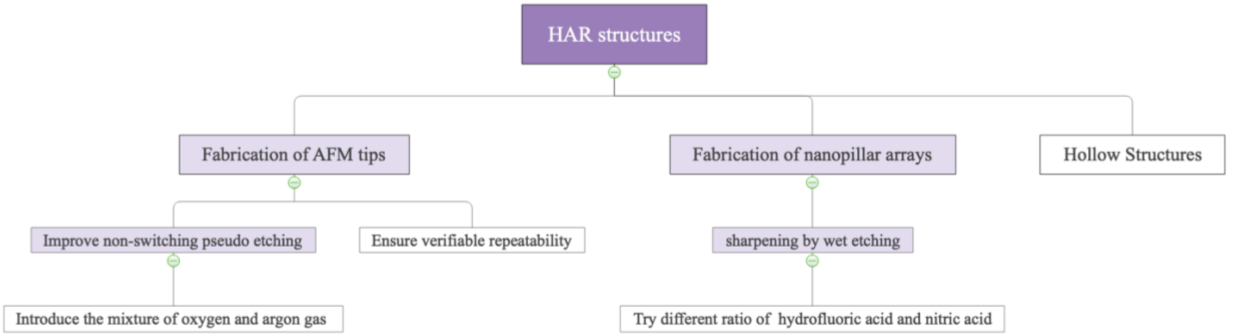

Figure 6.1 Conclusions and future works

Based on the experiences and findings of this project, there are several recommendations for future work in the field of fabrication of high aspect ratio structures as shown in Figure 6.1.

According to the fact that hollow microneedles with various tip diameters ranging from 10 to 50μm can smoothly penetrate skins, hollow nanoneedle can be fabricated to inject substance. Also, different conditions can be tested to improve the results. For example, the mixture of oxygen and argon gas can be introduced as cleaning step into plasma etching to observe the effect in non-switching pseudo-Bosch etching process, and different ratio of hydrofluoric acid and nitric acid can be applied to sharpen the structures. Lastly, it is important to ensure the repeatability and achieve quantity production of the fabrication.

References

[1] Lee, H., Xiong, Y., Fang, N., Srituravanich, W., Durant, S., Ambati, M., Sun, C., Zhang, X. (2005). Realization of optical superlens imaging below the diffraction limit. *New Journal of Physics*. Volume 7.

[2] Binnig, G., Rohrer, H., Gerber, Ch., Weibel, E. (1982). Surface studies by scanning tunneling microscopy. *Physics. Rev. Lett.* 49(1), p.57.

[3] Binnig, G., Quate, C. F., Gerber, C. (1986). Atomic force microscope. *Physics. Rev. Lett.* 56, 930.

[4] Scanning tunneling microscopy. *Nanoscience Instruments*. May 11, 2020 retrieved from https://www.nanoscience.com/techniques/scanning-tunneling-microscopy/.

[5] Temiryazev, A., Bozhko, S., Robinson, A.E., Temiryazeva, M. (2016). Fabrication of sharp atomic force microscope probes using *in situ* local electric field induced deposition under ambient conditions. *Review of Scientific Instruments 87, 113703.* Retrieved from https://doi.org/10.1063/1.4967457.

[6] Chung, K.H. (2014). Wear characteristics of atomic force microscopy tips: A reivew, *International Journal of Precision Engineering and Manufacturing*, vol. 15, pp. 2219.

[7] Henry, M.D., Walavalkar, S., Homyk, A. and Scherer, A. (2009). Alumina etch masks for fabrication of high-aspect-ratio silicon micropillars and nanopillars.

Nanotechnology, *20*(25), p.255305

[8] Review of progress in atomic force microscopy. (2020). *The Open Neuroimaging Journal.* Retrieved from https://benthamopen.com. Volume 13.

[9] Wang, Y.J. (2013). Constant Force Feedback Controller Design Using PID-Like Fuzzy Technique for Tapping Mode Atomic Force Microscopes. *Intelligent Control and Automation.* Vol. 4, No. 3. DOI:10.4236/ica.2013.43031

[10] Akiyama, K., Eguchi, T., An, T., Fujikawa, Y., Yamada-Takamura, Y., Sakurai, T. and Hasegawa, Y., (2005). Development of a metal–tip cantilever for noncontact atomic force microscopy. *Review of scientific instruments*. *76*(3), p.033705.

[11] Magonov, S. N., Elings, V., Whangbo, M.-H. (1997). Phase imaging and stiffness in tapping-mode atomic force microscopy. *Surface Science*. Volume 375, Issues 2-3, pg. L385-L391.

[12] Introduction to Bruker's ScanAsyst and PeakForce tapping AFM technology. Retrieved from https://www.bruker.com. Application note #133.

[13] Li, C., Ostadhassan, M., Guo, S., Gentzis, T., Kong, L. (2018). Application of PeakForce tapping mode of atomic force microscope to characterize nanomechanical properties of organic matter of the Bakken Shale. *Fuel.* Volume 233, pg. 894-910.

[14] Zheng, S., Zhu, C., Dey, K.R., Cui, B. (2017). Batch fabrication of AFM probes with direct positioning capability. *Journal of Vacuum Science & Technology B*. Retrieved from https://doi.org/10.1116/1.5010814

[15] Menozzi, C. et al. (2008). Focused ion beam as tool for atomic force microscope (AFM) probes sculpturing. *J. Phys.:Conf. Ser.* 126 012070.

[16] Lugstein, A., Bertagnolli, E., Kranz, C., Kueng, A., Mizaikoff, B. (2002). Integrating micro- and nanoelectrodes into atomic force microscopy cantilevers using focused ion beam techniques. *Applied Physics Letters 81.* 349; doi: 10.1063/1.1492304.

[17] Ageev, O.A., Kolomiytsev, A.S., Bykov, A.V., Smirnov, V.A., Kots, I.N. (2015). Fabrication of advanced probes for atomic force microscopy using focused ion beam. *Microelectronics Reliability 55.* pg. 2131-2134.

[18] NanoWorld AG, Neuchatel, Switzerland. Retrieved from www.nanoworld.com.

[19] High Aspect Ratio (> 10:1) - Non-Contact / Tapping Mode - High Resonance Frequency - Reflex Coating. Retrieved from www.nanosensors.com.

[20] Randolph, S., Fowlkes, J., Rack, P. (2006). Focused, nanoscale electron-beam-induced deposition and etching. *Critical Reviews of Solid State and Materials Sciences.* 31 (3): 55.

[21] Gordeev, S. (2012). Simple EBID process delivers robust nanoneedle AFM probe. Retrieved from nanotechweb.org.

[22] Nanda, G., van Veldhoven, E., Maas, D., Sadeghian, H. and Alkemade, P.F., 2015. Helium ion beam induced growth of hammerhead AFM probes. *Journal of Vacuum Science & Technology B, Nanotechnology and Microelectronics: Materials, Processing, Measurement, and Phenomena*, *33*(6), p.06F503.

[23] Shah, A.H. (2016). Applications of carbon nanotubes and their polymer nanocomposites for gas sensors. *Carbon Nanotubes - Current Progress of their Polymer Composites.* doi: 10.5772/63058.

[24] Lijima, S. (1991). Helical microtubules of graphitic carbon. *Nature 354.* p.g. 56-58.

[25] Jahanshahi, M., Kiadehi, A.D., (2012). Fabrication, purification and characterization of carbon nanotubes: Arc-discharge in liquid media (ADLM). *Syntheses and Applications of Carbon Nanotubes and Their Composites.* doi: 10.5772/5116.

[26] Carbon Nanotube Based AFM Probe. Nano Science & Technology. Retrieved from www.indiamart.com/nanosciencetechnology.

[27] Yazdanpanah, M.M., Harfenist, S.A., Safir, A., Cohn, R.W. (2005). Selective self-assembly at room temperature of individual freestanding Ag2Ga alloy nanoneedles. *J. Appl. Phys*. *98*, 073510.

[28] Retrieved from http://nauganeedles.com.

[29] Dey, R.K., Shen, J., Cui, B. (2017). Oxidation sharpening of silicon tips in the atmospheric environment. *Journal of Vacuum Science & Technology B* 35, 06GC0.

[30] He, H., Zhang, J., Yang, J., Yang, F. (2017). Silicon tip sharpening based on thermal oxidation technology. *Microsystem Technologies*. 23, p.1799-1803.

[31] Choudhury, R.P. (1997). Handbook of microlithography, micromachining and microfabrication. *IEE Materials and Devices Series 12*. Chapter 2: Electron beam lithography.

[32] Debnath, S., Kunar, S., Anasane, S.S., Bhattacharyya, B. (2017). Non-traditional micromachining processes: opportunities and challenges. *Materials Forming, Machining and Tribology*. p. 1-59.

[33] Hoole, A.C.F., Welland, M.E., Broers, A.N. (1997). Negative PMMA as a high-resolution resist- the limit and possibilities. *Semicond. Sci. technol*. p. 1166-1170.

[34] Duan, H., Xie, E., Han, L., Xu, Z. (2008). Turning PMMA nanofibers into graphene nanoribbons by in situ electron beam irradiation. *Advanced Materials*. 20, p. 3284-3288.

[35] Junarsa, I., Stoykovich, O.M., Nealey, F.P. (2005). Hydrogen silsesquioxane as a high resolution negative-tone resist for extreme ultraviolet lithography. *Journal of Vacuum Science & Technology B: Microelectronics and Nanometer Structures Processing, Measurement and Phenomena*. Volune 23, 138.

[36] Kretz, J., Dreeskornfeld, G., Ilicali, G., Lutz, T. (2005). Comparative study of calixarene and HSQ resist systems for the fabrication of sub-20 nm MOSFET device demonstrators. *Microelectronic Engineering.* Volumes 78–79, p. 479-483.

[37] Delft, van F.C., Weterings, J.P. (2000). Hydrogen silsesquioxane/novolak bilayer resist for high aspect ratio nanoscale electron-beam lithography. *Journal of Vacuum*

Science & Technology B: Microelectronics and Nanometer Structures Processing, Measurement, and Phenomena 18, 3419.

[38] Yang, H., Jin, A., Luo, Q., Li, J., Gu, C., Cui, Z. (2008). Electron beam lithography of HSQ/PMMA bilayer resists for negative tone lift-off process. *Microelectronic Engineering.* Volume 85, Issues 5-6, p. 814-817.

[39] Mancini, D.P., Gehoski, K.A., Ainley, E., Nordquist, K.J., Resnick, D.J. (2002). Hydrogen silsesquioxane for direct electron-beam patterning of step and flash imprint lithography templates. *Journal of Vacuum Science & Technology B: Microelectronics and Nanometer Structures Processing, Measurement, and Phenomena* 20, 2896.

[40] Toofan, M., Toofan, J. (2015). A brief review of the cleaning process for electronic device fabrication. *Developments in Surface Contamination and Cleaning.* p.185-212.

[41] Allen, D.M., Routiedge, I.A. (1983). Anisotropic etching of silicon: a model diffusion-controlled reaction. IEE proceedings (solid-state and electron device). Volume 130, Issue 2, p. 49-56. DOI: 10.1049/ip-i-1.1983.0012.

[42] Wu, B.Q., Kumar, A., Pamarthy, S. (2010). High aspect ratio silicon etch: A review. *Journal of Applied Physics* 108, 051101.

[43] Erickson, G.D. (2014). A Study of Anisotropic Chemical Etching on Crystalline Silicon. *Physics Capstone Project*. Retrieved from https://digitalcommons.usu.edu/phys_capstoneproject/7.

[44] Donnelly, V., Kornblit, A. (2013). Plasma etching: Yesterday, today, and tomorrow. *Journal of Vacuum Science & Technology A: Vacuum, Surfaces, and Films, 31*(5).

[45] Lee, Y. N., Schwartz, S. E. (1980). Reaction kinetics of nitrogen dioxide with liquid water at low partial pressure. *J. Phys. Chem.* 85, 840-848.

[46] Global Dry Etch Systems Market 2020 by Manufacturers, Regions, Type and Application, Forecast to 2026. (2020). Retrieved from https://surfacingmagazine.net/global-dry-etch-systems-market-2020-increased-prevalence-rate-with-topmost-players-by-2026-with-covid-19-scenario-ulvac-hitachi-high-technologies-plasma-therm-spts/.

[47] Fonash, J.S. (1990). An overview of dry etching damage and contamination effects. *Journal of The Electrochemical society.* Volume 137, No.12.

[48] Cirino, G.A., Barea, L.A.M., Mansano, R.D., Verdonck, P., Zuben, A., Frateschi, N.C., Diniz, J.A. (2019). Comparative study between wet and dry etching of silicon for microchannels fabrication. *Advanced Fabrication Technologies for Micro/Nano Optics and Photonics XII.* 1093015. Retrieved from https://doi.org/10.1117/12.2506804.

[49] Sycheva, A.A., Voronina, E., Rakhimova, V.T. (2018). Molecular dynamics simulation of physical sputtering of nanoporous silicon-based materials with low

energy argon. Journal of Surface Investigation X-ray Synchrotron and Neutron Techniques. 12(6): 1270-1277.

[50] Sigmund, P. (1987). Mechanisms and theory of physical sputtering by particle impact. *Nuclear Instruments and Methods in Physics Research Section B: Beam Interactions with Materials and Atoms*. Volume 27, Issue 1, p. 1-20.

[51] Important MEMS Processes. *Semiconductor Technology.* Retrieved from https://www.tf.unikiel.de/matwis/amat/semitech_en/kap_7/backbone/r7_2_2.html.

[52] Dain, G.L. (2017). Multiscale approach for simulation of silicon etching using SF_6/C_4F_8Bosch process. *Journal of Vacuum Science & Technology A 35,* 03E113.

[53] Addae-Mensah, K.A., Retterer, S., Opalenik, S.R., Thomas, D. Lavrik, N.V., Wikswo, J.P. (2009). Cryogenic etching of silicon: an alternative method for fabrication of vertical microcantilever master molds. *Microelectromech Syst.* Doi:10.1109/JMEMS.2009.2037440.

[54] Aydinoglu, F., Pan, A., Zhu, C., Cui, B. (2020). Effect of oxygen plasma cleaning on nonswitching pseudo-Bosch etching of high aspect ratio silicon pillars. *J. Vac. Sci. Technol. B* 38, 012804.

[55] Pgalajda, *Public Domain*, Retrieved from https://commons.wikimedia.org/w/index.php?curid=8999436.

[56] Con, C., Zhang, J., Cui, B. (2014). Nanofabrication of high aspect ratio structures using an evaporated resist containing metal. *Nanotechnology 25*, 175301.

[57] Saffih, F., Con, C., Alshammari, A., Yavuz, M. (2014). Fabrication of silicon nanostructures with large taper angle by reactive ion etching. *J. Vac. Sci. Technol. B,* 32, 06FI04.

[58] Ayari-Kanoun, A., Aydinoglu*,* F., Cui, B. (2016). Silicon nanostructures with very large negatively tapered profile by inductively coupled plasma-RIE. *J. Vac. Sci. Technol. B*, 34, 06KD01.

[59] Chen, L., Luciani, V., and Miao, H. (2011). Effect of alternating Ar and SF_6/C_4F_8 gas flow in Si nano-structure plasma etching. *Microelectronic Engineering 88,* 2470.

[60] Huang, Y., Lee, S.L., Thibeault, B.J., Coldren, L.A. (2011). Fabrication of highly ordered silicon nanowire arrays with controllable sidewall profiles for achieving low-surface reflection. *IEEE Journal of selected topics in quantum electronics*. 17, 869.

[61] Wang, X., Chen, Y., Wang, L., Cui, Z. (2008). Fabrication of nanoimprint template in Si with high etch rate by non-switch DRIE process**.** *Microelectronic Engineering 85*, 1015.

[62] Nishi, Y., Doering, R. (2007). Handbook of semiconductor manufacturing technology. 2nd edition. Chapter 15-7.

[63] Schaepkens, M., Oehrlein, G. S. (2001). A review of SiO2 etching studies in inductively coupled fluorocarbon plasmas. *Journal of The Electrochemical Society*. *148*(3), C211-C221.

[64] Kravetz, R. E. (2005). Hypodermic Syringe. *The American Journal of Gastroenterology.* 100(12), 2614-2615.

[65] Campbell, C. (2017). Dental Fear and Anxiety in Pediatric Patients. *Springer.* Chpt.12(2), 206-209.

[66] Romgens, A. M., Bader, D. L., Bouwstra, J. A., Baaijens, F. T., Oomens, C. J. (2014). Monitoring the Penetration Process of Single Microneedles with Varying Tip Diameters. *Journal of the Mechanical Behavior of Biomedical Materials*. Volume 40, 397-405.

[67] Lamichhane, N., et al. (2018). Liposomes: Clinical Applications and Potential for Image-Guided Drug Delivery. *Molecules.* 23(2): 288.

[68] Lundstrom, K. (2018). Viral Vectors in Gene Therapy. *Diseases.* 6(2): 42.

[69] Ain, Q.U., Jong, Lee, J.H., Woo, Y. S., Kim, T. H. (2016). Effects of Protein Transduction Domain (PTD) Selection and Position for Improved Intracellular Delivery of PTD-Hsp27 Fusion protein Formulations. *Archives of Pharmacal Research.* 39(9): 1266-1274.

[70] Reissmann, S. (2014). Cell Penetration: Scope and Limitations by the Application of Cell Penetrating Peptides. *Journal of Peptide Science*. Volume 20, Issue 10: 760-784.

[71] Kaushal, A. M., Gupta, P., Bansal, A. K. (2004). Amorphous Drug Delivery System: Molecular Aspects, Design, and Performance. *Therapeutic Drug Carrier Systems.* 21(3): 133-193.

[72] Chiappini, C., Almeida, C. Silicon Nanoneedles for Drug Delivery. *Semiconducting Silicon Nanowires for Biomedical Applications*. Page 144-167. (2014).

[73] Chen, C.Y., Wei, T. C., Lin, C. T., Li, J. Y. (2017). Enhancing Formation Rate of Highly Oriented Silicon Nanowire Arrays with the Assistance of Back Substrates. *Scientific Reports.*

[74] Shaoyuan, L., et al. Fabrication of Porous Silicon Nanowires by MACE Method in $HF/H_2O_2/AgNO_3$ System at Room Temperature. *Nanoscale Research Letters*. 9(1): 196. (2014).

[75] Matsumoto, D., et al. (2015). Oscillating High-aspect-ratio Monolithic Silicon Nanoneedle Array Enables Efficient Delivery Functional Bio-Macromolecules into Living Cells. *Scientific Reports.* 15325.

[76] Folch, A., Wrighton, M. S., Schmidt, M.A. (1997). Microfabrication of Oxidation-Sharpened Silicon Tips on Silicon Nitride Cantilevers for Atomic Force Microscope. *Journal of Microelectromechanical Systems.* Volume 6, No. 4.

[77] Obataya, I., Nakamura, C., Han, S.W., Nakamura, N., Miyake, J. (2005). Mechanical Sensing of the Penetration of Various Nanoneedles into a Living Cell Using Atomic Force Microscopy. *Biosensors and Bioelectronics*. Volume 20, Issue 8, 1652-1655.

[78] Robbins, H., Schwartz, B. (1959). Chemical Etching of Silicon I. *Journal of the electrochemical society*. 106, 505.

[79] Robbins, H., Schwartz, B. (1960). Chemical Etching of Silicon II. *Journal of the*

electrochemical society. 107, 108.

[80] Hamzah, A.A, Aziz, N.A., Majlis, B.Y., Yunas, J., Dee, C.F., Bais, B. (2012). Optimization of HNA etching parameters to produce high aspect ratio solid silicon microneedles. *Journal of Micromechanics and Microengineering*. Volume 22, Number 9.